Discovery of a 3.46 billion-year-old impact crater in Western Australia

Hiroshi Ohmoto[1*], Uschi M. Graham[2], Zi-Kui Liu[3], Yuya Tsukamoto[4,5], Yumiko Watanabe[4], Hiroshi Hamasaki[6] and Andrew Chorney[7].

[1]: Dept. of Geosciences, The Pennsylvania State University, University Park, PA 16802 USA.

[2]: Dept. of Pharmaceutical Sciences, University of Kentucky, Lexington, KY 40508 USA.

[3]: Dept. of Material Sciences and Engineering, The Pennsylvania State University, University Park, PA 16802 USA.

[4]: Dept. of Earth Sciences, Tohoku University, Sendai 980, Japan.

[5]: Atmosphere and Ocean Research Institute, The University of Tokyo, Chiba, 277-8564, Japan

[6]: Tokyo Gas Co., Ltd., Minato-ku, Tokyo 105-8527, Japan.

[7]: Dept. of Earth Sciences, Temple University, Philadelphia, PA 19122, USA

*Corresponding author: hohmoto@psu.edu

Current models for the origin and constituents of Earth are based primarily on compositions of meteorites that fell recently (within the past ~1 million years) on Earth. Here we report the discovery of a probable crater (~150x100x3 km in the original dimension), which was possibly created by the impact of a large (~10 km in diameter) asteroid on a >2.5 km-deep, oxygenated ocean-floor in Pilbara, Western Australia 3.46 billion-years (Ga) ago; that is, more than 1.2 Gyr earlier than the oldest known impact crater on Earth. This discovery was made mostly through a drone-assisted survey of the

distributions of impact breccias and tsunami deposits. We have also discovered numerous micro-fragments (<1 μm to ~3 mm in sizes) of the asteroid (named here as "The Apex Asteroid") in tsunami deposits and submarine pillow lavas that were most likely generated by the asteroid impact. The micro-fragments are mostly comprised of titanite ($CaTiSiO_5$) and rutile (TiO_2), and frequently associated with native iron (Fe), carbon (C)-rich nanocrystals (e.g., SiC, graphite), coesite (high-pressure polymorph of SiO_2) and a variety of alloys, such as iron-iridium (Ir) alloys with up to ~10 wt% Ir, iron-nickel (Ni)-cobalt (Co)-, aluminum (Al)-copper (Cu)-, Al-Si-, Si-C-, Fe-C- and C-Al-Ca-Cu-Fe alloys. The Apex Asteroid was much richer in titanium (Ti), calcium (Ca) and vanadium (V), and poorer in magnesium (Mg) and Fe compared to recently-fallen meteorites. Thermochemical analyses of the asteroid minerals suggest that: (1) the parental planetary body of the Apex Asteroid condensed from a solar-gas cluster that was hotter and having higher H_2/H_2O and H/O ratios compared to planetary bodies for the recently-fallen meteorites; (2) it may represent a major building-block of Earth; and (3) Earth and the Moon have the same chemical and isotopic compositions, but Ti atoms in the Earth's magma oceans partitioned into the Ti-rich core and Ti-poor mantle, while most Ti atoms in the lunar magma oceans condensed as the Ti-rich mantle.

Current models for the origin and constituents of Earth postulate that its core is composed primarily of Fe-Ni alloys with minor Si and S, such as found in Fe- and/or stony-Fe meteorites; whereas the mantle resembles the compositions of stony meteorites, such as CI-carbonaceous chondrites[1,2], ordinary chondrites[3] or enstatite chondrites[4], which are composed primarily of Mg-Fe-rich and Ti-Ca-poor silicates. These meteorites fell mostly within the last ~1 million year

48 (Myr) [5], and referred to here "modern meteorites". However, questions remain as to whether
49 the Earth's building blocks ~4.56 Ga ago are truly represented by "modern meteorites" [6,7]. For
50 example, recognizing the differences in some elemental ratios (e.g., Al/Si, Mg/Si, Fe/Mg) and
51 isotopic ratios of elements (e.g., O, Re and Nd) between the estimated "primitive Earth mantle"
52 and various chondrites, Drake and Righter[6] have suggested "The 'building blocks' of the Earth
53 must instead be composed of unsampled 'Earth chondrite' or 'Earth achondrite'. The oldest
54 meteorite falls are the 2.7 Gyr-old iron micro-meteorites discovered in carbonate beds in Pilbara,
55 Australia [8]. The oldest-terrestrial-aged stony meteorites, recovered from ~466 Ma-old
56 limestone beds in Sweden and China, are found to be much significantly richer in Ti (i.e., ~2
57 wt% vs. <0.3 wt%), and have distinctly different abundance ratios of various types of chondrites
58 and achondrites than any "modern meteorites" [9,10].
59 Impact history of the Moon[11] suggests frequent bombardments of asteroids on early Earth.
60 Evidence of asteroid impacts on early Earth, such as impact spherules (i.e., terrestrial rocks
61 vaporized by asteroid impacts and condensed as melts) and Ir-rich sedimentary rocks, has been
62 found in several sedimentary-rock formations ~3.47-3.25 Ga and ~2.7-2.5 Ga in ages [12-16].
63 However, no stony-meteorite fragments older than ~466 Ma [9,10] or impact crater older than
64 ~2.2 Ga in ages [17,18] has been found on Earth.
65 In 2003, the NASA Astrobiology Program carried out a series of drillings in the Eastern
66 Pilbara district of Western Australia (Fig. 1) to recover some of the oldest geologic formations
67 for investigations aimed at understanding the evolution of life and environment on early Earth.
68 The first drilling (ABDP #1)[19] recovered a 264 m-long continuous drill core that encompasses
69 the youngest section of the Duffer Formation (submarine felsic volcanic formation of ~3.46 Ga
70 in age), a ~150 m section of the Marble Bar Chert Member (MBCM, chert/jasper unit) and a ~70

m earliest-section of the Apex Basalt (submarine komatiite/basalt pillow lavas) (Fig. 1d & Fig. 2a). At the 2017 Goldschmidt Conference, we[20] reported the discovery of numerous (>1,000) mineral fragments (<1 μm to ~3 mm in sizes), which we interpreted as fragments of a meteorite (or asteroid), throughout the ~70 m section of the Apex Basalt in the ABDP #1 core. These "meteoritic" mineral fragments are comprised mostly of titanite ($CaTiSiO_5$) and rutile (TiO_2). Our report, however, met with some skeptics, because: (i) such Ti-rich minerals are extremely rare in "modern meteorites", (ii) meteoritic minerals have not been reported in a submarine lava of any geologic age, and (iii) titanite and rutile are common hydrothermal-alteration products of submarine basalts.

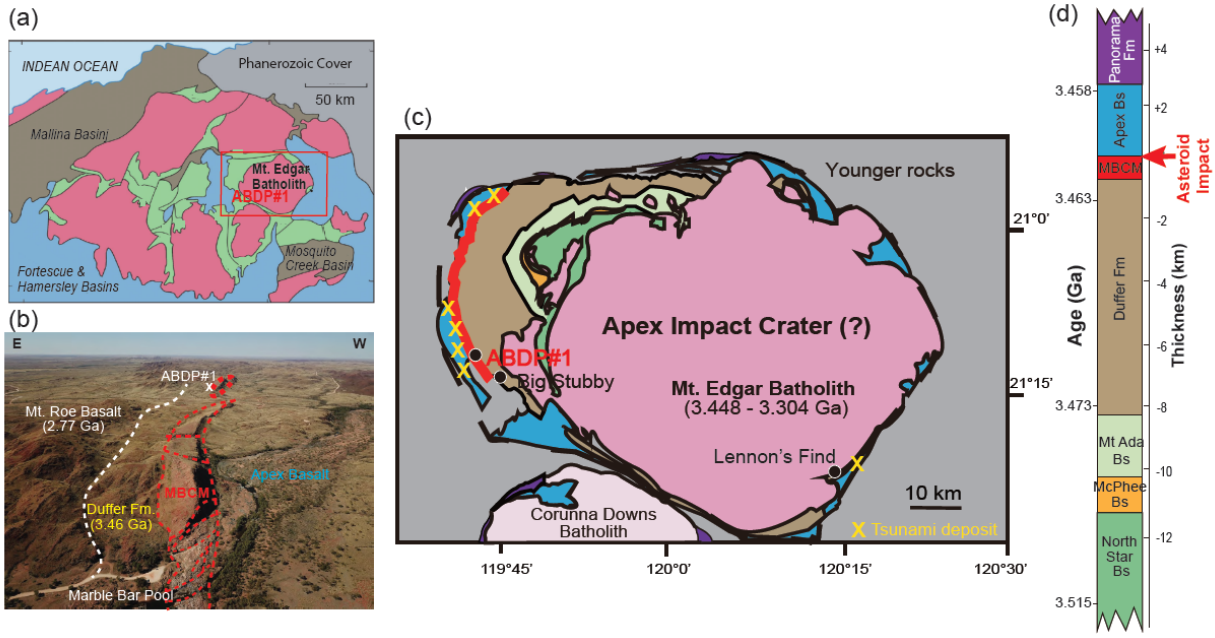

Figure 1. Geologic settings of the proposed Apex Impact Crater. (a): Simplified geologic map of the East Pilbara Craton (modified after Hickman[21,22]); greenstone belts in green and granitoid batholiths in dark pink. (b): Aerial (drone) photo of the Marble Bar Chert Member (MBCM) from ~500 m above the ground. The distance from the Marble Bar Pool to the ABDP #1 drilling site is about 2.5 km. Note that the MBCM was broken into ~50-500 m-sized blocks, probably by the shock waves generated by an asteroid impact. (c): Geologic map of the proposed Apex Impact Crater (modified after the Geologic Map of the Pilbara East by the Geological Survey of Western Australia[22]). The Big Stubby and Lennons Find are Cu-rich volcanogenic massive sulphide (VMS) deposits in the Duffer Formation. (d): Stratigraphic column of the geologic formations in the proposed Apex Impact Crater (modified after [22]).

Subsequently, we have continued various types of investigations of the "meteoritic grains" and their geological and geochemical environments (see "*Methods*") and concluded that the semi-circular structure, presently ~80x65 km (but originally ~150x100 km) in size and encompassing the ~3 km-thick Apex Basalt and the Mt. Edgar Granite Batholith (Figs. 1-a & -c), likely represents a crater created by impact of a large (~10 km in diameter) asteroid, which produced the "meteoritic" fragments discovered in the Apex Basalt (Figs. 2-a & -b). Below we present various types of observations and data that have lead us to the above conclusions.

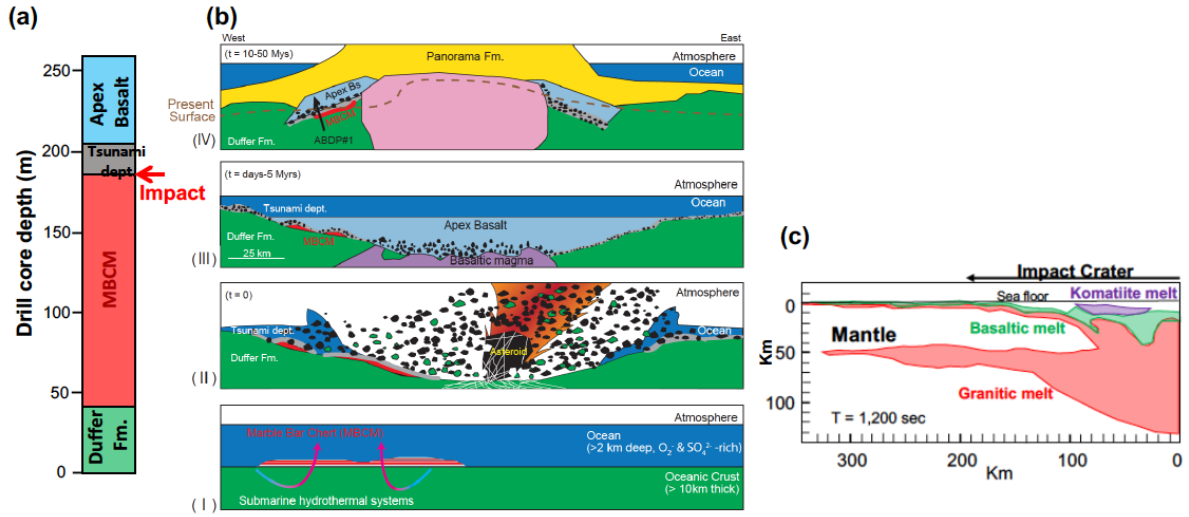

Figure 2. History of the Apex Impact Crater. (See A in *Methods*). (a). A stratigraphic column of the ABDP #1 drill core. (b). The sequence of major events in the impact crater. (I): Pre-impact sage. (II): An impact of a ~10 km-sized asteroid on the deep ocean floor, causing: brecciation and fragmentation of the asteroid, the MBCM and the Duffer Formation; generation of tsunami currents and deposition of tsunami deposits. (III): Mantle impact melting and eruption of the Apex Basalt magmas. (IV): Emplacement of the Mt. Edgar granite batholith and eruptions of the Panorama volcanic rocks. (c): Impact melting of an oceanic crust and the mantle by a 30 km-sized bolide (modified after Jones[23]).

Impact breccias and tsunami deposits

The MBCM is a ~20-200 m-thick, steeply dipping and slightly overturned chert/jasper unit that outcrops continuously ~20 km along a strike in the western part of the proposed Apex Impact Crater (Figs. 1 b-c; Fig. 3a). Previous researchers recognized an abundance of highly-unsorted "chaotic" sedimentary rocks that contained angular fragments of the MBCM and occurring between the well-bedded MBCM and overlying Apex Basalt. These features were described as "turbidites interbedded with debris-flow deposits" by DiMarco & Lowe[24], or as "mixed conglomerate beds, chert breccia beds and chert folded beds of the MBCM" and interpreted as the product of high-density turbidity currents and mass-transport complexes in

channels-levees in deep-sea fans by Olivier et al.[25]. However, the virtual absence of round fragments of the MBCM in the "chaotic zone" is difficult to explain by these detrital-sediments models.

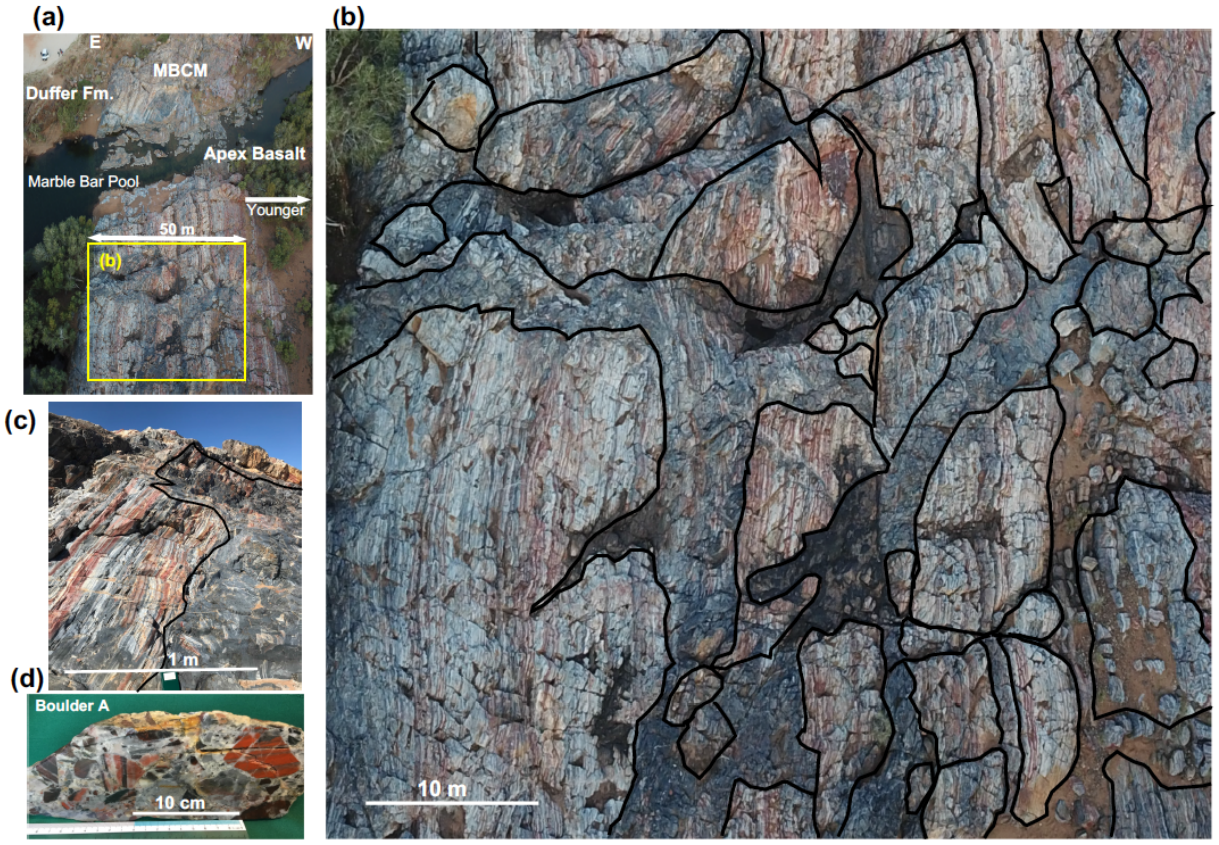

Figure 3. Asteroid impact structures in the Marble Bar Chert Member (MBCM). (a): An aerial view (looking south from ~250 m above the ground) of the MBCM in a ~100x50 m area at the Marble Bar Pool. (b): A close-up view of area (b) (~50x40 m area) in Fig. (a). Note the abundance of fractures (up to ~5 m wide) that are oblique to the bedding planes, various-sized (up to ~10 m) broken and rotated blocks and angular fragments of the MBCM, and gray/black "muds" (i.e., tsunami sediments) that intruded into the fractures and gaps between the MBCM fragments. (c): An outcrop photo of the impact-induced tsunami deposits, containing ~1 cm to ~5 m-sized fragments of the MBCM. (d): A boulder of tsunami deposits, containing angular fragments of red-, black- and white cherts in the matrix comprised mostly of powdered MBCM and the Duffer Formation.

Our drone-assisted field survey, which focused mostly on a ~4 km area along the strike of the MBCM around the Marble Bar Pool (Figs. 1 b-c), revealed an abundance of brecciations, displacements, deformations, disturbances and impact metamorphism of the MBCM and the Duffer Formation from <1 μm to ~1 km in scales (Figs. 1b; Figs. 3 a-d; Extended Data (ED) Figs. 1 a-k; ED Figs. 2 a-k). An entire section of the ~20-200 m-thick MBCM was broken into

various-sized, sharp-edged fragments and blocks, which were displaced by up to ~10 m-wide fractures that cross-cut the MBCM bedding planes at high angles. Gaps between the blocks and fragments were filled with black/gray-coloured "muds" that contained various-sized angular fragments, pulverized chert and -volcanic rocks (from the Duffer Formation), and "inclusions" and "intrusions" of basalts up to ~2 m-thick and ~10 m-long. Soft-sediment deformation features of the bedded MBCM are common.

Through detailed mapping of a ~40x20 m area of the MBCM at the Marble Bar Pool, Oliver & Cawood[26] recognized essentially the same features described above and interpreted them as products of tectonic activity and the dewatering of partially-consolidated MBCM. However, we interpret that aforementioned structural and textural features in the MBCM represent impact breccias (in-site- and fallback breccias) that were created by shock waves from an asteroid impact, because of the abundance of shock-metamorphic features in the MBCM and Duffer Formation (ED Figs. 2 a-k) and of meteoritic minerals in the "mixed zone" (i.e., tsunami deposits) and the Apex Basalt (ED Figs. 3 a-t; see later section). Pillow basalts with inclusions of chert fragments are common (ED Figs.1 b-k; ED Figs. 2 b-e). These features indicate that a bolide impacted before the consolidation of the upper parts of the MBCM, and that eruptions of the first >50 m of the ~3 km-thick Apex basalt began essentially concurrent to the depositions of fragmented-, crashed- and powdered cherts. In areas in the eastern parts of the proposed Apex Impact Crater where the MBCM did not form, boulders and fragments of the volcanic Duffer Formation are mixed with powdered volcanic rocks in the tsunami deposits (ED Fig. 1k).

Meteoritic minerals in pillow basalts and tsunami deposits

***Titanite and rutile*:** The most abundant "meteoritic" grains (>95 % of the total "foreign" grains) in the Apex Basalt and tsunami deposits are Ca-Ti-Si-O-rich phases (referred to here as

"Ti-rich grains") that are comprised mostly of titanite and rutile (Figs. 4 a-h; ED Figs. 3 a-t). These grains are virtually free of Fe (Supplementary Table 2), indicating that they were not formed by alteration of Ti-rich iron-oxides by Ca-rich hydrothermal solutions (see reaction R-1 in *Method*), such as those found in some submarine basalts[27, 28]. Titanite crystals and basalts in the hydrothermally-altered zone of the ABDP #1 core are characterized by losses of essentially all the Ca atoms by submarine hydrothermal fluids (ED Figs. 4 b, i, l, & m) (see reaction R-2 in *Method*), indicating that the Ti-rich grains are exotic minerals (e.g., meteorite fragments) which were incorporated in the pillow basalts and tsunami deposits before submarine hydrothermal alteration.

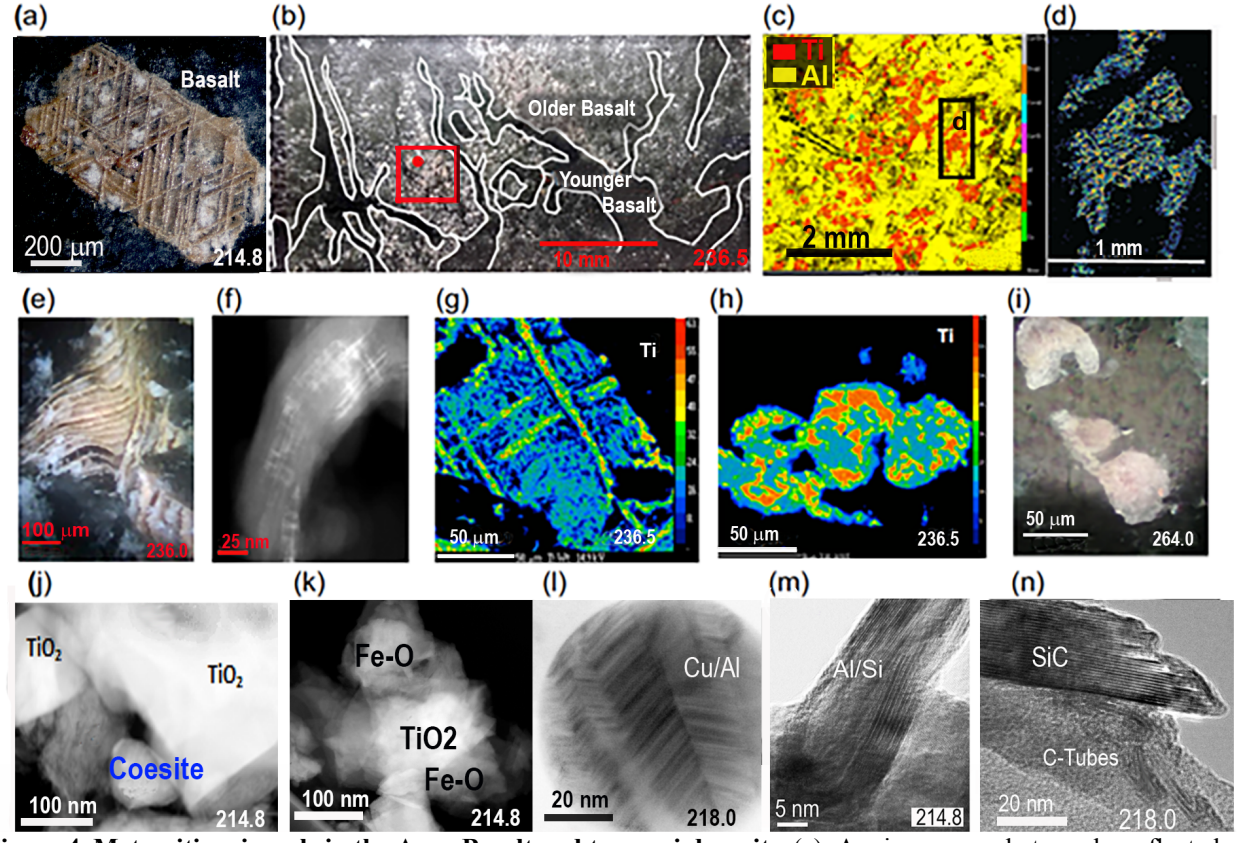

Figure 4. Meteoritic minerals in the Apex Basalt and tsunami deposits. (a): A microscope photo under reflected light of the first meteoritic mineral fragment discovered in the Apex Basalt. Due to the reactions with oxygenated submarined hydrothermal fluids, rutile (TiO_2)-rich lamellae and haematitized (brown-coloured) surfaces have became distinct. (b): A thin section photo (under reflected light) of a drill-core chip of the Apex Basalt, showing abundant Ti-rich asteroid fragments (khaki colour) in the older basalt flows, but virtually absent in the younger flows. (c): A composite EMPA maps of Ti (red; asteroid fragments) and Al (yellow; basalt) in area (c) in Fig. (b). (d): An EPMA map of Ti map for area (c) in Fig. (c). (e): Thin section photo (under reflected light) of a Ti-rich

fragment with bent crystal structure, which was possibly created by a planetary collision. (f): A HAADF image of the bent crystal lattice shown in (e). (g): An EPMA map of Ti in a Ti-rich fragment, showing the titanite-rich matrices (blue), titanite- and rutile-rich lamellae (dark green) and rutile crystals (yellow & red). (h): An EPMA map of Ti in Ti-rich melt spherules. (i): A thin section photo (under reflected light) of melted Ti-rich spherules. (j)-(n): STEM photos of meteoritic minerals associated with Ti-rich fragments.

The Ti-rich grains (Figs. 4 a-i; ED Figs. 3 a-t; Figs. g-j) are characterized by: (a). angular, irregular and ragged shapes and the virtual absence of rounded grains, eliminating the possibility of a detrital origin; (b). virtual absence of reaction rims; (c). large variation in the grain size (<1 μm to ~3 mm); (d). heterogeneous distributions in the basalt lavas (Fig. 4b): highly abundant (~1 to ~5 volume %) in older basalt melts that crystallized probably in contact with seawater, but virtually absent in younger lavas that infiltrated the older basalts and probably not in contact with seawater; (e). secondary fragmentation of the grains, possibly by ablation by other crystals, during incorporation/transportation in basalt lavas, as suggested by the jigsaw puzzle-like matching of neighboring fragments (ED Fig. 3b); and (f). association with the minerals that have been found in common chondrites and achondrites, such as iridium (Ir)-rich minerals, Fe-Ni-Co alloys, Al-Si alloys, silicon carbide (SiC) and various forms of carbon (e.g., graphene, carbon nanotubes) (Figs. 4 j-n; ED. Figs. 7-9). Characteristics (a)-(f) indicate that the Ti-rich grains did not crystalize either as primary- or secondary (alteration) minerals of the basalt lavas or tsunami deposits, but they were incorporated in the basalt lavas and tsunami deposits as foreign materials from the ocean water. Because the solubilities of Ti-bearing minerals in aqueous solutions are extremely low[29], the Ti-rich compounds in the seawater must have existed as solid suspensions/deposits (i.e., asteroid fragments). Characteristics (a)-(f) can be best explained by the fragmentation of an outer zone of an asteroid body as it impacted to a deep-ocean floor. The asteroid fragments, together with vaporized terrestrial rocks and chert fragments, were ejected from the impact site on an ocean floor into the overlying ocean and atmosphere as impact clouds,

and then fell back to the ocean (see Fig. 2b). The Stokes' Law suggests that it would take ~4 days, ~400 days, and ~100 years, respectively, for titanite grains of 100 μm, 10 μm, and 1 μm in diameters to sink through a ~5 km-column of calm ocean water. However, tsunami waves would have mixed and stirred them, especially inside the impact crater, to deposit widely heterogenous Ti-rich grains and tsunami deposits. The tsunami waves within a large impact crater may have lasted for more than several days [30], and eruptions of the Apex Basalt possibly began within a few hours of the impact (see A-III in *Method*), therefore explaining why both the tsunami deposits and at least the first 50 m section of the Apex Basalt contain various-sized Ti-rich grains (Figs. 4 a-c; ED Figs. 3 a-t). It should also be noted that the maximum stability temperatures of titanite + rutile assemblage (> ~1,100 °C at ~1 atm)[31] are higher than the basalt lava temperatures (~1,000 – 1,150°C)[32], explaining why most of the titanite-rutile grains were not melted in the basalt lavas. But some Ti-rich grains have melted to form Ti-rich spherules (Figs. 4 h-i; ED Figs. 5 a-d), possibly by a planetary collision of the parental body with another planet or by the heat in the impact clouds.

The Ti-rich angular fragments are also characterized by: (g). exsolution textures with rutile (TiO_2)-rich lamellae and titanite ($CaTiSiO_5$)-rich matrices (i.e., between lamellae) (Fig. 4g; ED Figs. 3 a-t); (h). aggregates of nanometer-sized crystals of titanite and rutile that comprise the lamella and matrices (Fig. 4g; Extended Data Figs. 3 f-t); and (i). distorted crystal lattice structures (Figs. 4 e-f; ED Figs. 3 c-e). These features suggest the following sequence of events for the parental planetary body of the Apex Asteroid: (1) condensation of nano-sized crystals of Ti-rich crystals from the solar gases during the formation of the parental planet; (2) reorganization of the nano-crystals of Ti-rich minerals to form larger (>10 μm in size) crystals with rutile-rich lamellae and titanite-rich matrices during cooling of the parental body; and (3)

223 deformation of crystal lattice of the Ti-rich crystals by a collision of the parental body with
224 another planetary body. The Ti-rich spherules with rutile-rich lamellae and titanite-rich matrices
225 (Fig. 4 h-j; ED Figs. 5 a-d) were possibly formed by melting of angular Ti-rich fragments,
226 followed by slow cooling to develop the exsolution textures while in impact clouds. The basaltic-
227 spherules (ED Figs. 5 e-h) and wiggled-shaped silica (ED Figs. 5 i-k) were probably condensed
228 in the impact cloud from vaporized volcanic rocks of the Duffer Formation and chert of the
229 MBCM, respectively.

230 Analyses of some rutile crystals by EELS (electron energy loss spectroscopy) indicate the
231 presence of both Ti^{3+} and Ti^{4+} (ED Figs. 6 a-c)[33]; some Ti^{3+} atoms may have been Ti^{2+} before
232 entering in the Earth's atmosphere (see later "Discussions").

233 ***Metallic Fe and Fe-oxides*:** Metallic iron and Fe-oxide crystals are intimately associated
234 with the Ti-rich crystals in the pillow basalts (Fig. 4 j-k). Fe-oxides are also found as discrete
235 grains in the tsunami deposits (ED Figs. 7 l-p). They vary from euhedral crystals (hexagonal,
236 octahedral) to irregular shaped crystals. Their Fe/O atomic ratios (ED Figs. 7 l-p; ED Figs. 8 i-j;
237 Supplementary Table S3) suggest that the original grains were metallic Fe (Fe/O atomic ratios
238 >>1) and possibly wüstite (Fe/O = 0.95-0.88) as well. Some grains, especially at the margins,
239 exhibit lower Fe/O ratios (e.g., ~0.75 for magnetite and 0.67 for haematite; Supplementary
240 Table S3), possibly due to partial oxidation while in the high-temperature impact clouds in the
241 O_2-rich ocean and atmosphere and/or by O_2-rich submarine hydrothermal fluids. The abundant
242 fragments of red cherts (Fig. 3d; ED Fig. 7k) in the tsunami deposits are unequivocal evidence
243 that the formation of the primary hydrothermal haematite crystals in the MBCM took place in the
244 O_2-rich deep oceans prior to the asteroid impact at ~3.46 Ga, rather than by recent ground water
245 (see A-I in *Methods*).

246 It has been debated whether the native iron and Fe-C alloys in Tertiary-aged basalt lavas in
247 the Disko Island are meteorite origin or products of the assimilation of C-rich rocks (e.g., coal),
248 causing the $Fe^{2+}O$ component in basalt melts to be reduced by carbon [34, 35]. However, C-rich
249 sedimentary rocks (e.g., black shales) are absent in pre-3.5 Ga geologic formations in the Pilbara
250 district, eliminating the possibility of a terrestrial origin for the Fe-metal and wüstite in the Apex
251 Basalt.

252 ***Iridium-rich minerals****:* As many meteorites are Ir-rich, researchers[12-16] have used Ir-rich
253 sedimentary layers as evidence for the contemporaneous impacts of asteroids (or large
254 meteorites) somewhere on Earth. In the tsunami deposits and pillow basalts, Ir is enriched in
255 three groups of meteoritic minerals: Ir-Fe-(Ni) alloys, Al- and REE (rare earth element)-enriched
256 phosphates, and zircon (see Table S4 in Supplementary Information). Their Ir contents vary from
257 <0.05 % (i.e., detection limit) to ~10 wt.% (Fig. 5a; ED Figs. 8 c-k), which matches the highest
258 Ir content previously reported for meteorites (i.e., inclusions in the Ornance carbonaceous
259 chondrites[36]).

260 ***Other alloys*****:** Submicron-sized crystals of Ni-Cr-Co alloys, spherules of Al-Cu with
261 exsolution textures (Fig. 4l), Al-Si alloys (Fig. 4m) and C-Al-Ca-Si-Cu-Fe alloys (ED Figs. 9 k-
262 o) are found in the pillow basalts. The Al-rich alloys are similar to those discovered in the
263 recently-fallen Khatyrka meteorite[37, 38] and those in the "Hypatia"[39].

264 ***Carbon-rich phases****:* The C-rich phases associated with Ti-rich grains in the pillow basalts
265 occur in various forms (Fig. 4n; ED Figs. 9 a-o): graphite, graphene, carbon nanostructures (nano
266 tubes, nano spherules, nano whisker) and silicon carbide (SiC) crystals, which often contain 1-2
267 nanometer-sized native metal- or metal-oxide particles. These C-rich phases have been found in
268 a variety of meteorites [40-44]. Synthesis of carbon nanostructures and silicon carbide are

commonly carried out in laboratories via a variety of vapor deposition methods, in which C-rich gas (e.g., CO, hydrocarbons) is reduced by metal catalysts (e.g., Fe, Ni, Co, Pt) [45, 46]. Therefore, the question remains as to whether some (or all) of the C-rich phases were condensed in the Solar Nebula or re-condensed from the vaporized carbonaceous matter of the asteroid in impact clouds.

***Coesite**:* Silica-rich micron-sized crystals in some basalt samples (Fig. 4j) were identified by electron diffraction method as coesite, a high-pressure (>2 GP) polymorph of SiO_2 [47]. Because of its intimate association with meteoritic minerals (e.g., TiO_2, native Fe and Fe-Ni-Cr-Co alloys), this coesite was possibly produced by the shock metamorphism of quartz, crystobalite or tridymite in the parental planetary body upon collision with another planetary body or upon impact of the asteroid to Earth.

Discussion on the origins of the Apex Asteroid, Earth and the Moon

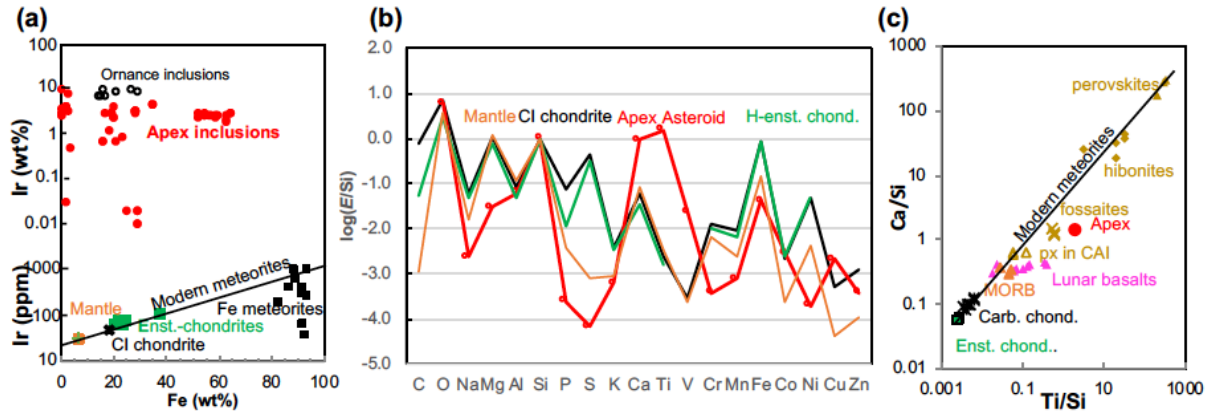

Figure 5. Chemical compositions of the Apex Asteroid. (a): Iridium contents of some meteoritic grains in the Apex Basalt, compared to other meteorites. (b): Comparisons of the elemental abundances (normalized to Si) in the Apex Asteroid with those in CI-chondrite, H-enstatite chondrite and the primitive mantle [48]. (c): Ti/Si and Ca/Si ratios of the Apex Asteroid are compared with those of CAI minerals (perovskites, hibonites, fossaites and pyroxenes), carbonaceous chondrites, H-enstatite chondrites, Earth mantle and lunar basalts [48-51], indicating that the Apex Asteroids and lunar basalts have much higher Ti/Si ratios compared to the other materials.

289 The asteroid fragments discovered in the Apex Basalt and tsunami deposits are all micro
290 fragments (<1 μm - 3 mm in size). It is possible that many other minerals beside the Ti-rich
291 minerals, such as pyroxenes, olivines and feldspars, had existed in the Apex Asteroid, but these
292 mineral fragments had been vaporized in the impact clouds and/or melted in the Apex Basalt
293 lavas, if their melting temperatures were less than ~1,100°C. However, because the abundances
294 of other phases (e.g., carbon and metal compounds) are less than ~1 volume % of the Ti-rich
295 grains and of the absence of identifiable other meteoritic mineral phases, we have assumed that
296 the bulk composition of the Apex Asteroid may be approximated by that of the least-altered Ti-
297 rich phases by observing. Based on EPMA analyses of 219 spots on Ti-rich grains
298 (Supplementary Table S2) and the estimated abundance ratio of (85±5)/(15±5) for the
299 matrix/lamellae, we have estimated the average compositions of the bulk Ti-rich grains (Table 1)
300 as $(Ca_{.74\pm.18}, Fe_{0.03\pm0.03})(Ti_{1.27\pm.17}, Al_{0.05\pm0.05}, V_{0.02\pm0.01}, Si_{0.81\pm.18})O_5$, if we assume that all the Ti
301 atoms are Ti^{4+}. Compared to all the stony meteorites investigated previously, the Apex Asteroid
302 is significantly enriched (>10 times) in Ti, Ca and V, significantly depleted (<1/10) in Mg, P, S,
303 Fe and Ni, and moderately to slightly depleted (~1/10 to ~9/10) in Cr and Mn, when normalized
304 to Si (Fig. 5b). The Ti/Si - Ca/Si relationships of the Apex Asteroid resemble those of calcium-
305 aluminum-rich inclusions (CAIs) (Fig. 5c). However, the Ti/Si ratios of the Apex Asteroid and
306 lunar basalts are much higher than those of the CAIs and "modern" meteorites, suggesting the
307 genetic relationships between the Apex Asteroid and the Moon (see later discussions).

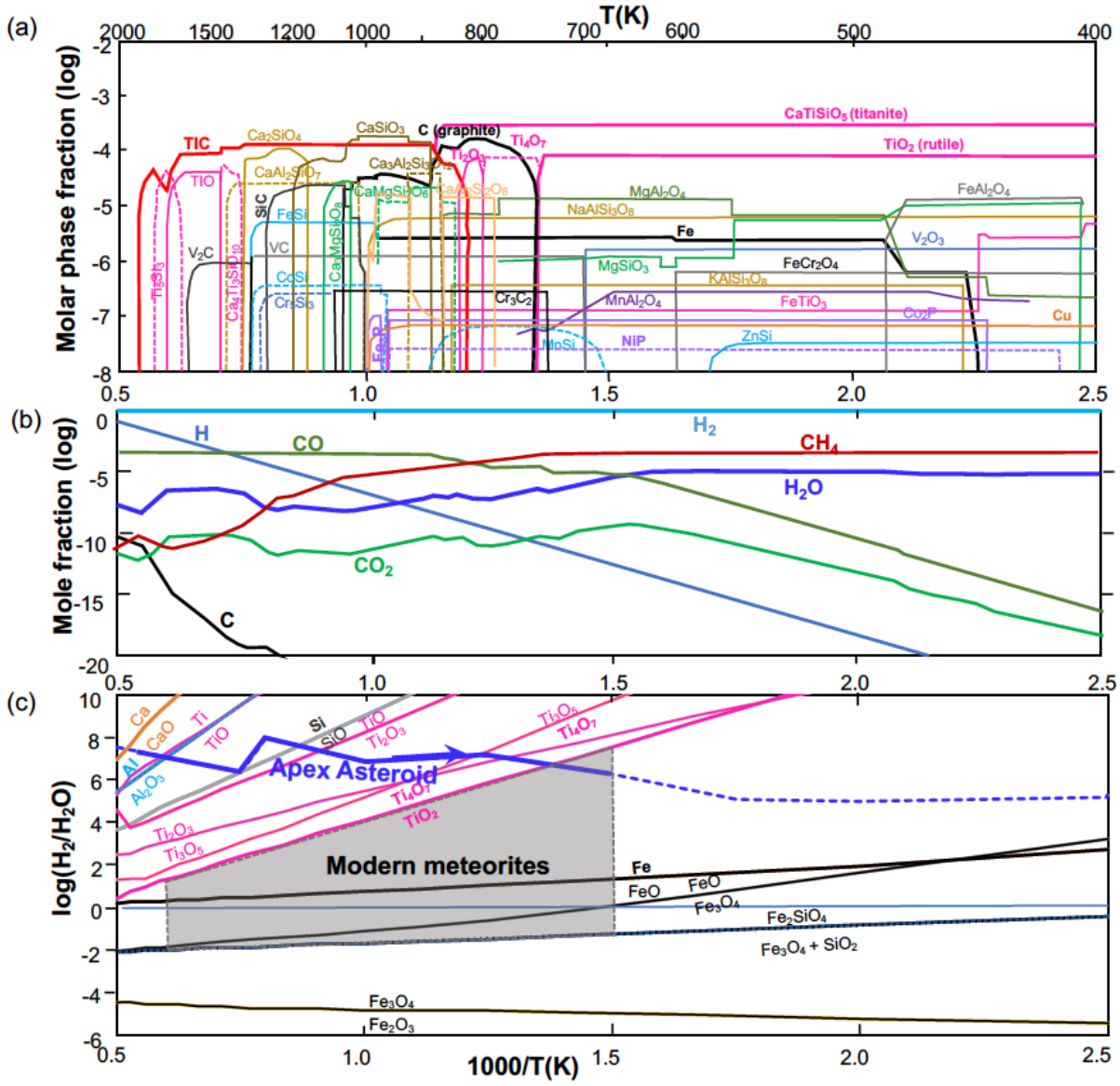

Figure 6. Thermochemical analyses of formation conditions of the Apex Asteroid (See C-7 in *Methods*)**.** (a): Temperatures of the appearances and disappearances of minerals from "the Apex solar-gas cluster" with the initial total gas pressure of 10^{-4} atm (see Supplementary Table 6). The red and pink lines represent Ti-rich minerals; black and gray lines for C- and/or Fe-rich minerals; blue lines for silicides; yellow and khaki lines for Ca-Al-rich minerals; green lines for Mg-rich silicates; and purple lines for phosphides. (b): Changes in the abundances of major gaseous species in the Apex solar-gas cluster during the formations of phases in (a). (c): Stability relationships among some redox-sensitive minerals as a function of H_2/H_2O ratio of the coexisting vapor phase. The blue line is for the Apex solar-gas cluster from (b); the gray area represents the redox-temperature conditions for the "modern" meteorites.

Assuming that ~4.6 Ga ago, the Solar Nebula had the same elemental ratios as the current Solar Wind and CI-carbonaceous chondrites, some researchers, such as Grossman[52] and Lodders[1], compute the condensation temperatures of meteoritic minerals by using

thermodynamic data. By adopting a similar thermochemical approach, we have computed the condensation-, transformation- and disappearance temperatures of solid phases and the abundance ratios of gaseous species during the cooling of a hypothetical solar-gas cluster that has the elemental ratios of the Apex Asteroid (Table 1), and the same H/C/Si ratios of the current Solar Photosphere and the initial total vapor pressure of 10^{-4} atm as Lodders[1] (see C-7 in *Methods*).

The results of our computations (Figs. 6a-c; Supplementary Table 6) differ significantly from those by Lodders[1], including: (1). The first major minerals to condense were the CAI minerals at 1,680-1,520K in Lodders[1], but Ti-carbides and -silicides at ~1,800K in this study. (2) Ti-bearing minerals in Lodders' are all oxidized (Ti^{4+}) compounds, but our calculations show that he first Ti-rich minerals condensed Ti^0-rich minerals, which successively transformed to compounds with higher valences, Ti^{2+}-rich, Ti^{3+}-and finally to Ti^{4+}-rich minerals at ~900-700K. (3). In our system, C-bearing solid phases initially condensed as carbides (e.g., TiC, FeC, SiC) at ~1830-1250K, which were transformed to C (graphite) at ~1040 K and decomposed to CH_4 (methane) at 730K. In contrast, no C-bearing solid phases condensed in Lodders system, except for $CH_4 \cdot 7H_2O$ (methane hydrate) at <400K. (4) Many native metals (and their alloys), such as Fe, Cu and Co, mostly condensed at ~980-900K. These data agree well with the observed occurrences of reduced compounds, such as graphite, carbon nanocrystals, FeC, Fe-rich alloys (Fe-Ir, Fe-Cu-Co-Ni) and Ti^{3+} in the Apex Asteroid. (5). Phosphorus (P) condensed as phosphides (P^0) of heavy metals (e.g., FeP, Ni_3P_2), rather than as phosphates (P^{5+}). (6) H_2/H_2O ratios of the Apex solar-gas cluster remained nearly constant at $10^{7\pm1}$ at ~2000-800 K. In contrast, H_2/H_2O ratios of the current Solar Photosphere and the gas clusters in equilibrium with the "modern" meteorites would be ~10^{-2}-10^{+6}, because the Fe in these meteorites occurs predominantly as Fe^{2+}-rich

344 minerals (e.g., Fe_2SiO_4, $FeSiO_3$) as well as native Fe, and Ti occurs essentially as Ti^{4+}; that is,
345 these H_2/H_2O values are much lower (i.e., more oxidized) that those of the Apex solar-gas cluster
346 (Fig. 6c). The major reason for such large differences in the results of computations stems from
347 the difference in the estimated abundance of oxygen atoms in the systems: the H/O atomic ratio
348 of 4,300 in our system vs. 1,750 in Lodders[1].

349 Most models for the origins of planets in the Solar system are based on an unspoken
350 assumption that the compositions of solar gases have remained the same as the current Solar
351 Winds. However, Barcall et al. [53] have estimated that at 4.57 Ga ago the Solar radius was
352 ~87% of today, luminosity ~70%, temperature ~97%, hydrogen mass fraction ~50% and
353 neutrino fluxes <10% of today. These estimates suggest that during the planet formations ~4.6
354 Ga ago elemental and isotopic compositions of the clusters of gases emitted from the early Sun
355 varied greatly from the present values. That is, the parental planetesimal for the Apex asteroid
356 (termed here as "Planetesimal A") condensed from solar-gas clusters with different chemical and
357 isotopic compositions from those for the "modern meteorites". The proto Earth was possibly
358 created by the accumulations of various planetesimals, not by a single type of planetesimal. For
359 example, a 50% mixture of Planetesimals A and the parental planetesimal for the enstatite
360 chondrites would have yielded the Earth's bulk compositions as Ti = ~10 wt%, Ca = ~8 wt%,
361 Mg = ~5 wt%, Fe = ~15 wt%, Ni = ~0.8 wt%, Si = ~8 wt%, Al = ~0.5 wt%, S = ~3 wt%, Si = ~
362 15 wt% and O = ~33 wt%. Impacts of other planetesimals to Planetesimal A during the Earth
363 formation would have ejected fragments of Planetesimal A into space; one of which returned to
364 Earth 3.46 Ga ago as the Apex Asteroid.

365 The current popular model for Earth and Moon formation postulates that the heat generated
366 from the conversion of kinetic energy from planetesimal accumulation and from the radioactive

decay of short-lived isotopes caused the entire Earth to melt and form magma oceans, and that the impact of Mars-size Theia ejected some of this magma ocean into space to form the Moon at 4.51 Ga [54]. Recently, Lock et al.[55] have proposed that the collision of Theia and the proto-Earth would have vaporized both planets and created a fast-spinning vaporized state (termed "synestia") and that magma oceans formed on Earth and the Moon as the synestia cooled. Both models for Moon's formation imply that the bulk compositions of Earth and the Moon are the same, yet the present mantles differ significantly, most likely due to the partitions of some elements into their respective cores. The changes in the mantle compositions would have been more significant for Earth, because the mass fraction of its core is about 32% [48], compared to less than 2% for the Moon [56, 57]. Under the reducing conditions of the initial magma oceans, Ti atoms could have existed as Ti^0, Ti^{2+} and Ti^{3+}as well as Ti^{4+} (see Fig. 6c). They would have reacted with Fe^0 in the magma oceans to form titanium-iron alloys and wüstite (FeO), such as:

$$TiO_{2(m)} + 3Fe^0_{(m)} = TiFe_{(m)} + 2FeO_{(m)} \quad (1)$$

Similarly, SiO_2 in the magma oceans would have formed FeSi and FeO by:

$$SiO_{2(m)} + 3Fe^0_{(m)} = FeSi_{(m)} + 2FeO_{(m)} \quad (2)$$

where subscript *m* refers to melt. The Ti-Fe and Si-Fe alloys would have sunk to the bottom of the magma oceans to create a metallic core, while the $FeO_{(m)}$ concentrated in the mantle, reacted mostly with $SiO_{2(m)}$ to form ferrous silicates. As a result, the remaining magma oceans on the early Earth would have become Ti-poor, FeO-rich, and its redox state (H_2/H_2O) became below that of the Fe/FeO buffer line. In contrast, the lunar mantle remained Ti-rich, retained near the initial Fe^0/Fe^{2+} ratio at about the Fe/FeO buffer line. This model explains why the lunar basalts generally contain much higher amounts of Ti than terrestrial basalts (average 3 wt% vs. ~1 wt%)[56,57]. It also suggests that the reason the Earth's core has a lower density than pure Fe metal

may not be due to the additions of H, Si, O and/or S to the core, as suggested in the current paradigm[58], but likely due to the significant additions of Ti and Si.

Similar to the impact history of the Moon[10], asteroid impacts on early Earth must have been much more frequent than during the Proterozoic and Phanerozoic Eons. This study suggests why impact craters older than ~2.2 Ga have not been found on Earth. Throughout the geologic history, most of the impact craters must have been created on deep-ocean floors rather than on land. Most of them subducted into the mantle, but some may have been thrusted up to the continental crust before being subjected to erosion. Therefore, many more Archaean-aged impact craters should be found in greenstone/granite terranes, such as those in the Pilbara Craton (Fig. 1a).

Table 1. EPMA analyses of Ti-rich grains in the Apex Basalt

Element	**Matrix (n = 39) wt.%**	**2σ**	**Lamellae (n = 21) wt. %**	**2σ**	**Bulk wt. %**	**2σ**
O	38.59	3.65	38.67	2.17	38.60	3.3
Na	0.12	0.51			0.1	0.5
Mg	0.57	1.14			0.48	0.9
Al	1.29	2.09			1.09	
Si	11.97	2.16	2.40	2.15	10.53	2.1
P	0.01	0.01			0.01	
S	0.01	0.01			0.01	
K	0.01	0.02			0.01	
Ca	16.14	4.27			13.71	3.6
Ti	22.87	6.67	57.27	3.68	28.03	6.2
V	0.35	0.21			0.30	0.2
Cr	0.01	0.01	0.53	0.29	0.08	0.1
Mn	0.02	0.04			0.02	
Fe	1.39	1.78	0.65	0.25	1.3	
Co	0.10	0.01			0.1	
Ni	0.01	0.02			0.01	
Cu	0.05	0.02			.04	
Zn	0.01	0.02			0.01	
Total	93.51	3.47	99.52		94.4	

n: The number of spots analyzed, excluding the data on more than 100 spots with mixed mineralogy and/or those altered by submarine hydrothermal fluids).

References

1. Lodders, K. Solar system abundances and condensation temperatures of the elements. *Am. J. Sci.* **591**, 1220-1247 (2003).
2. McDonough, M.F. Compositional model for the Earth's core. In *The Crust* (ed. Rudnick, R.L.), *Treatise on Geochemistry* (eds. Holland, H.D.& Turekian, K.K.) **3**, 559-565 (Elsevier, Amsterdam, 2005).
3. Allegre, C.J., Poirier, J-P, Humler, E. & Hofmann, A.W. The chemical composition of the Earth. *EPSL.* **134**, 515-526 (1995).
4. Javoy, M. et al. The chemical composition of the Earth: Enstatite chondrite models. *EPSL.* **293,** 259-268 (2010).
5. Nishizumi, K., Elmore, D. & Kubik, P.W. Update on terrestrial ages of Antarctica meteorites. *EPSL* **93,** 299-313 (1989).
6. Drake, M.J. & Righter, K. Determining the composition of the Earth. *Nature* **416,** 37-44 (2002).
7. Campbell, I.H. & O'Neil, H.S.G. Evidence against a chondritic Earth. *Nature* **483**, 553-553 (2012).
8. Tomkins, A. G. et al. Ancient micrometeorites suggestive of an oxygen-rich Archaean atmosphere. *Nature* **533**, 235-238 (2016).
9. Schmitz, B. et al. A new type of solar-system material recovered from Ordovician marine limestone. *Nature Communication* DOI: 10.1038/ncomms11851(2016).
10. Heck, P.R. et al. Rare meteorites common in the Ordovician period. *Nature Astronomy* **1**, 1-6 (2017).

11. Fernandes, V.A. et al. The bombardment history of the Moon as recorded by ^{40}Ar-^{39}Ar chronology. *Meteorites & Planetary Sci.* **48,** 241-269 (2013).

12. Lowe, D., Byerly, G.R. & Kyle, F.T. Recently discovered 3.42-3.23 Ga impact layers, Barberton Belt, South Africa: 3.8 Ga detrital zircons, Archean impact history, and tectonic implications. *Geology* **42**, 747-750 (2014).

13. Schulz, T. et al. New constraints on the Paleoarchean meteorite bombardment of the Earth – Geochemistry and Re-Os isotope signatures of spherule layers in the BARB5ICDP drill core from the Barberton Greenstone Belt, South Africa. *Geochim. Cosmochim. Acta* **211,** 322-340 (2017).

14. Glikson, A.Y., Allen, C. & Vickers, J. Multiple 3.47-Ga-old asteroid impact fallout units, Pilbara Craton, Western Australia. *ESPL.* **221**, 383-396 (2004).

15. Glikson, A. et al. A new ~3.46 Ga asteroid impact ejecta unit at Marble Bar, Pilbara Craton, Western Australia: A petrological, microprobe and laser ablation ICPMS study. *Precamb. Res.* **279**, 103-122 (2016).

16. Rasmussen, B. Iridium anomalies and shocked quartz in a late Archean spherule layer from the Pilbara craton: New evidence for a major asteroid impact at 2.63 Ga. *Geology* **32**, 1029-1032 (2004).

17. Reynold, W.U. & Gibson, R.L. Geology and evolution of the Vredefort Impact Structure, South Africa. *J. of African Earth Sci.* **23**, 125-162 (1996).

18. Erickson, T.M. et al. Precise radiometric age establishes Yarrabubba, Western Australia, as Earth's oldest recognized meteorite impact structure. *Nature Comm.* https//doi.org/101038/s41467-019-13985-7 (2020).

19. Hoashi, M. et al. Primary haematite formation in an oxygenated sea 3.46 billion years ago. *Nature Geosc.* **1**, 1-6 (2009).

20. Graham, U.M., Liu, Zi-K. & Ohmoto, H. ~3.4 Ga-old meteorite fragments suggest the Earth's core is rich in Ti, Si and Ca. Golschmidt 2017 Abstract 1412 https://goldschmidtabstracts.info/program/conferenceSeriesAuthorIndex?letter=A (2017).

21. Hickman, A.H. Review of the Pilbara Craton and Fortescue Basin, Western Australia: Crustal evolution providing environments for early life. *Island Arc* **21**, 1-31 (2012).

22. Hickman, A.H. Interpreted bedrock geology of the east Pilbara Craton. Scale: 1:250000. *Geol. Survey of Western Australia* (2016).

23. Jones, A.P. Modeling impact volcanism as a possible origin for the Ontong Java Plateau. *Geol. Soc. Am. Sp. Paper* **388,** 711-720 (2005).

24. DiMarco, M.J. & Lowe, D.R. Shallow-water volcanic deposition in the Early Archean Panorama Formation, Warrawoona Group, eastern Pilbara Block, Western Australia. *Sed. Geol.* **64,** 43-63 (1989).

25. Olivier, N. et al. A deep subaqueous fan depositional model for the Paleoarchaean (3.46 Ga) Marble Bar Cherts, Warawoona Group, Western Australia. *Rapid Comm.* Doi:10.1017/S0016756812000131 (2012).

26. Oliver, N.H.S. & Cawood, P.A. Early tectonic dewatering and brecciation on the overturned sequence at Marble Bar, Pilbara Craton, Western Australia: dome-related or not? *Precamb. Res.* **105,** 1-15. (2012).

27. Kitajima, K., Maruyama, S., Utsunomiya, S. & Liou, J. G. Seafloor hydrothermal alteration of an Archean mid-ocean ridge. *J. Metamorphic Geol.* **19**, 583-599 (2001).

28. Hansen, E., Reimink, J. & Harlov, D. Titaniferous accessary minerals in very low-grade metamorphic rocks, Keweenaw Peninsula Michigan, USA. *Lithos* **116**, 167-174 (2010).

29. Stumm, W. & Morgan, J.J. *Aquatic Chemistry* 3rd Ed. (John Wiley & Sons, New York, 1996).

30. Wünnemann, K., Weiss, R. & Hofmann, K. Characteristics of oceanic impact-induced large water waves – Re-evaluation of the tsunami hazard. *Meteoritics & Planet. Sci.* **42,** 1893-1903 (2007).

31. Hellman, P.L. & Green, T. The role of sphene as an accessary phase in the high-pressure partial melting of hydrous mafic compositions. *EPSL* **42,** 191-201 (1979).

32. Moore, J.G. Mechanism of formation of pillow lavas. *Amer. Scientist* **63,** 269-277 (1975).

33. Stoyanov, E., Langenhorst, F. & Steinle-Neumann, G. The effect of valence state and geometry on Ti $L_{3,2}$ and O *K* electron energy-loss spectra of Ti_xO_y phases. *Am. Mineralogist* **92,** 577-586 (2007).

34. Pauly, H. White cast iron with cohenite, schreibersite, and sulphides from Tertiary basalts on Disko, Greenland. *Medd. Dansk Geol. Foren. København.* Bind **19**, 8-26 (1969).

35. Goodrich, C. A. & Bird, J. M. Formation of iron-carbon alloys in basaltic magma at Unifaq, Disko Island: the role of carbon in mafic magmas. *J. Geol.* **93**, 475-492 (1985).

36. Palme, H., Wlotzka, F., Nagel, K. & El Goresy, A. An ultra-refractory inclusion from the Ornana carbonaceous chondrite. *EPSL* **61**, 1-12 (1982).

37. MacPherson, G.J. et al. A new CV3 find from the Koryak Mountain, Eastern Russia. *Meteor. Planet. Sci.* **48**. 1499-1514 (2014).

38. Bindi, L. et al. Evidence for the extraterrestrial origin of a natural quasicrystal. *PNAS* **109.** 1396-1401 (2012).

39. Belyanin, G.A. et al. Petrography of the carbonaceous, diamond-bearing stone "Hypatia" from southwest Egypt: A contribution to the debate on its origin. *Geochim. Cosmochim. Acta* **223**, 462-492 (2018).

40. Rubin, A.E. Mineralogy of meteorite groups. *Meteoritics & Planetary Science* **32**, 231-247 (1997).

41. Buseck, P.R. & Bo-Jun, H. Conversion of carbonaceous material to graphite during metamorphism. *Geochim. Cosmochim. Acta* **49,** 2003-2016 (1985).

42. Leung, I., Guo, W., Friedman, I. & Gleason, J. Natural occurrence of silicon carbide in a diamondiferous kimberlite from Fuxian. *Nature* **346**, 352- 354 (1990).

43. Heymann, D. et al. Terrestrial and extraterrestrial fullerenes. *Fullerenes, Nanotubes, and Carbon Nanostructures **11**,* 444-370 (2003).

44. Garvie, L.A.J. & Buseck, P.R. Nanosized carbon-rich grains in carbonaceous chondrite meteorites. *EPSL* **224**. 431-439 (2004).

45. Dai, H. Carbon nanotubes: Synthesis, integration and properties. *Acc. Chem. Res.* **35**, 1035-1044 (2002).

46. Szabó, A. et al. Synthesis methods of carbon nanotubes and related materials. *Materials* **3,** 3092-3140 (2010).

47. Saika-Voivod, I., Sciortino, F., Grande, T. & Poole, P.H. Phase diagram of silica from computer simulation. *Physical Review E* **70**, 061507 1-8 (2004).

48. Henderson, P. & Henderson, G.M. *The Cambridge Handbook of Earth Science Data* (Cambridge Press, Cambridge, 2009).

49. MacPherson, C.J. Calcium-aluminium-rich inclusions in chondritic meteorites. In *The Meteorites, Comets, and Planets* (ed. Davis, A.M.), *Treatise on Geochemistry* (eds. Holland, H.D.& Turekian, K.K.) **1,** 201-246 (Elsevier, Amsterdam, 2005).

50. E.K. Zinner. Presolar grains. In *The Meteorites, Comets, and Planets* (ed. Davis, A.M.), *Treatise on Geochemistry* (eds. Holland, H.D.& Turekian, K.K.) **1,** 17-39 (Elsevier, Amsterdam, 2005).

51. Krot, A.N. & Keil, K. Anorthite-rich chondrules in CR and CH carbonaceous chondrites: Genetic link between calcium-aluminum-rich inclusions and ferromagnesian chondrules. *Meteor. Planet. Sci.* **37**, 91-111 (2002).

52. Grossman, L. Condensation in the primitive solar nebula. *Geochi. Cosmochim. Acta* **36,** 597-619 (1972).

53. Bahcall, J.N., Pinssonneault, M.H. & Basu, S. Solar models: current epoch and time dependences, neutrinos, and helioseismological properties. *Astrophys. J.* **555,** 990-1012 (2001).

54. Barboni, M. et al. Early formation of the Moon 4.51 billion years ago. *Science Adv.* **3,** e1602365 (2017).

55. Lock, S. et al. The origin of the Moon within a terrestrial Synestia. *J. Geophys. Research: Planets.* **123,** 910-951(2018). 10.1002/2017JE005333.

56. de Vries, J., van den Berg, A. & van Wesrenen. W. Formation and evolution of a lunar core from ilmenite-rich magma ocean cumulates. *EPSL* **292,** 139-147 (2010).

57. Taylor, S.R. The Moon re-examined. *Geochim, Cosmochim. Acta* **141,** 670-676 (2014).

58. Hirose, K. et al. Crystallization of silicon dioxide and compositional evolution of the Earth's core. *Nature* **543,** 99-102 (2014).

539
540 ***Methods***
541
542 **A. Methods for unravelling the geologic history of the Apex Impact Crater**
543 Glikson et al. [15] reported the discovery of two zones of impact-spherule-rich layers in the
544 Marble Bar Chert Member (MBCM) of the Duffer Formation at 57-58 m and 77 m depths in the
545 ABDP #1 drill core. Each zone contains multiple spherule-rich layers that are ~1-5 cm in
546 thickness and packed with nearly uniform-sized (1-2 mm diameters) spherules with Mg-Fe-Ca-
547 rich core (possibly basaltic in composition) and secondary siderite-rich rims. The spherule-rich
548 layers are interbedded with diamictite layers, which were most likely formed by impact-
549 generated tsunami currents and comprised of variable-sized (<1 mm to ~10 cm) angular chert
550 fragments. These impact spherules were correlated to the 3,472-3,470 Myr-old impact spherule
551 units in the Barberton Greenstone Belt in South Africa. Because of the uniformity in the spherule
552 sizes and the absence of accompanying meteorite fragments, these small spherules and tsunami
553 deposits were probably generated by asteroid impacts at >500 km away, much like those found
554 in the Lake Superior region from the 1.8 Ga Sudbury Impact [59, 60].
555 In contrast, fragments of "meteoritic minerals" discovered by us in a ~70 m section (~190 to
556 ~264 m depth interval) of the Apex Basalt in the ABDP #1 drill core greatly vary in size (<1 μm
557 to ~ 3mm), shape and abundance (Figs. 4 a-i; ED Figs. 3 a-t). The associated diamictite zone is
558 tens of meter thick, containing large fragments (up to ~10 m in size) (Figs. 3 a-d; ED Figs. 1 a-
559 k). These observations have lead us to hypothesize that: the Apex Asteroid impacted to the ocean
560 floor near (within ~100 km of) the ABDP #1 site during the accumulation of the MBCM; and the
561 semi-circular igneous structure, presently ~80 km E-W and ~65 km N-S in size and centered at S
562 21°10' and E 120°0' (Fig. 1c), may represent the asteroid impact crater, termed here "the Apex
563 Impact Crater". This is one of the eight greenstone-granite complexes that characterize the
564 geology of the Eastern Pilbara Craton (Fig. 1a). As the rock formations in the "Apex Impact
565 Crater" are generally ~60°-80° tilted (overturned), mostly due to the deformation associated with
566 the intrusion of granite batholiths, the initial dimensions were much larger, possibly ~150 km (E-

567 W) and ~100 km (N-S). Below are the proposed sequence of events in the Apex Impact Crater
568 (see Fig. 2b).

569 **A-I: Geological and geochemical environments before the asteroid impact**: Submarine
570 volcanic rocks of the Warrawoona Group, which includes the North Star Basalt-, McPhee
571 Basalt-, Mt. Ad Basalt-, and Duffer Formations (Fig. 1d), are more than 13 km in thickness and
572 accumulated without a subaerial-erosional surface during a ~55 Myr period (3,515-3,460 Ma
573 ago) [21]. Because of its great thickness and long period of submarine volcanism, we suggest
574 that the Warrawoona Group, comprised mostly of basalt and komatiite lavas and minor
575 dacite/rhyolite lavas, represented an oceanic crust that formed on a mid ocean ridge. The
576 occurrences of felsic igneous rocks (rhyolite and dacite) in mid ocean ridges were possibly
577 similar to those found on Iceland today; they may have formed by fractional crystallization of
578 basaltic magmas and/or by the partial melting of hydrothermally-altered oceanic crust [61]. The
579 occurrences of Cu-rich volcanogenic massive sulfide deposits (VMS; the Lenners Find- and the
580 Big Stubby deposits; see Fig. 1c) in the upper part of the Duffer Formation suggest that the
581 seawater depths were greater than ~2.5 km (i.e., P_{H2O} > ~250 bars), because Cu-rich submarine
582 hydrothermal fluids, which are typically 300-400 °C in temperatures, must discharge on the
583 seafloor without boiling in order to form Cu-rich massive sulfide ores [62]. In fact, Samieyani[63]
584 obtained homogenization temperatures of 250-390 °C for fluid inclusions with no evidence of
585 boiling in barite and quartz crystals from the Big Stubby deposits near Marble Bar.

586 The MBCM (~20-200 m thick) is a low-grade Algoma-type Banded Iron Formation,
587 characterized by alternating microbands of white-coloured silica-rich chert, red-coloured
588 haematite-rich jasper, and black-coloured magnetite-rich jasper[19]. Based on detailed
589 mineralogical and geochemical investigations utilizing a variety of electron microscopes, Hoashi

et al.[19] have recognized that the primary haematite crystals are typically submicron-sized (~0.1-0.6 μm) euhedral crystals (ED. Figs. 7 g-j), which most likely formed by rapid mixing of Fe^{2+}-rich hydrothermal fluids with O_2-rich cold deep-ocean water at T ≥ 60°C on or near the seafloor:

$$2Fe^{2+}_{(hyd.\ fl.)} + 1/2O_{2(sw)} + 2H_2O \rightarrow Fe_2O_{3(hm)} + 4H^+ \quad \text{(R-1)}$$

If the ferric-iron oxides had formed at temperatures below ~60°C, they would have been goethite ($Fe(OH)_3$), rather than haematite[19]. Based on these observations, they have concluded that the ocean-atmosphere system was already fully oxygenated ~3.5 Ga ago. However, based on an interpretation of Pb isotope data on some basalt samples from the ABDP #1 core, Li et al.[64] concluded that the additions of uranium (U) and O_2 to the Apex Basalt occurred by modern O_2-rich groundwater, not by the 3.46 Ga seawater, implying that the haematite crystals did not form 3.46 Ga ago. Focusing on the larger (>10 μm), subhedral secondary haematite crystals in the MBCM, Rasmussen et al.[65] also suggested that all haematite crystals, including the submicron-sized haematite crystals, formed though the oxidation of Fe^{2+}-rich minerals, such as siderite ($FeCO_3$) and magnetite (Fe_3O_4) by recent groundwater. However, they have neglected the photographic evidence, presented by Hoashi et al.,[19] showing that siderite and magnetite crystals in the haematite-rich red bands of the MBCM clearly grew from the submicron-sized primary haematite crystals (ED Figs. 7 i-j), which were subsequently converted to large secondary haematite crystals. Furthermore, various geochemical characteristics of the Apex Basalt in the hydrothermally-altered zone, such as the negative Ce anomalies, the increased contents of Ba, U and Fe^{3+} and $Fe^{3+}/\sum Fe$ and U/Th ratios (ED Figs. 7 b-f), indicate that the 3.46 Ga submarine hydrothermal fluids developed from the O_2-, SO_4^{2-}- and U rich seawater [66].

A-II. The asteroid impact and associated events: The Apex Basalt, which overlies the MBCM, is ~3 km-thick (Fig. 1d), comprised of submarine basalt/komatiite lavas with abundant

613 pillow structures (ED Fig. 1i). Recognizing that the MBCM in the studied drill core is highly
614 fractured, brecciated, and interfingering with basalts, especially in the upper section (i.e., deeper
615 in the drill core), we suggest (see Fig. 2b) that: (i) an asteroid body impacted to the ocean floor
616 near (within ~100 km of) the ABDP #1 site during the accumulation of the MBCM, and created
617 a large impact crater; (ii) shock waves generated by the impact shattered, brecciated, dislocated,
618 locally overturned the chert blocks, and generated large tsunami currents, especially in areas
619 inside the crater, which formed thick (~5-30 m) tsunami deposits; (iii) upon impact, the asteroid
620 fragmented into various-sized pieces, which were blown into the overlying ocean and
621 atmosphere, and subsequently fell back (i.e., fallback breccia) on the tsunami deposits and the
622 pillow basalts, primarily inside of the impact crater. The geometry of the impact crater was most
623 likely defined by the outcrop-areas and thickness (~3 km) of the Apex Basalt. Therefore, the
624 original impact crater was a semi-circular in shape, ~150 km (E-W) and ~100 km (N-S) in size,
625 ~3 km deep from the surrounding ocean floor and ~5-6 km deep from the sea level. Size of the
626 impactor, according to an equation for the ratio of crater/impactor sizes[67], would have been ~10
627 km in diameter.

628 **A-III. Generation and eruptions of the Apex Basalt magmas:** The proposed Apex Impact
629 Crater is about a half the size of the Ontong Java Plateau. Some researchers[23,68] have suggested
630 that the Ontong Java Plateau, the world's largest oceanic plateau, was created by magmas that
631 were generated by the impact of a ~30 km-diameter asteroid to a deep ocean floor ~120 Ma ago.
632 According to the simulations by Jones[23], the impact of a ~30-km diameter asteroid created a
633 crater ~400 km in diameter, and caused mantle melting to depths of ~150 km almost
634 instantaneously (i.e., < ~10 minutes) by impact heating of the oceanic crust and by sudden
635 decompression melting of deeper mantle (Figs. 2 b-c). The degree of melting of the mantle

peridotite would have decreased with increasing depth: from ~100 % at <~20 km depths, >50% at <~70 km depths and >1% at <~150 km depths. Melts formed from ~100 % melting of peridotite would be komatiitic[69], while those from ~50 % and ~5% partial melting would produce basaltic magmas and granitic magmas, respectively [70]. These depths of melting would be shallower when the impact asteroids were smaller.

Analogous to the ascent speeds of kimberlite magmas[71], the komatiite/basalt melts generated by impact melting of the mantle could have risen with the speeds of ~10-30 m/sec through the mantle fractures created by the impact. Thus, within one hour of the impact, komatiite/basalt lavas would have erupted into the impact crater to form the Apex Basalt. According to the simulations[72], tsunami currents generated by impact of a ~10 km-diameter asteroid would have risen more than a few kilometers in heights and lasted for more than a day, especially within the impact crater. Such a prolonged tsunami event and the rapid eruptions of basalt/komatiite lavas would explain the intimate associations of basalts and chert fragments in the tsunami deposits and in the early phases of the Apex Basalt (ED Figs. 2 b-e). Since the Apex Asteroid impacted to a deep ocean floor, and the "impact plumes" were possibly confined mostly within the ocean (rather than dispersed into the atmosphere), large tsunami currents would have stirred fragments of various sizes and densities in the water column inside the impact crater. This would explain the extremely large size-variation in asteroid fragments in the Apex Basalt and tsunami deposits. Volume of the Apex Basalt lavas in the proposed Apex Impact Crater would be ~$5x10^5$ km^3, assuming an original dimension of ~150 km diameter and ~3 km depth; this is approximately the same volume as a typical LIP (large igneous province) (>10^5 km^3)[73].

A-IV. Generation and emplacements of the granitoid magmas: A large granite body typically occurs in the central parts of impact craters on Earth, such as the 2.0 Ga Vredefort[17]

and ~60 Ma Chixulub Crater[74]. These granite bodies may represent the rebound of the lower continental crust, as these asteroids impacted on a thick continental crust. Granitoid batholiths in the Apex Impact Crater (i.e., the Mt. Edgar Granite Batholiths) are, however, similar to those in the 1.8 Ga Sudbury Impact Crater[75], as they intruded as granitic magmas through the earlier mafic/ultramafic igneous bodies. Crystallization ages of the granite complex in "the Apex Crater" range from ~3,448 to ~3,426 Ma [21], indicating that the first granite intrusive occurred at ~10 Myr after the impact event at ~3,460 Ma, and that the granite intrusive events lasted for ~20 Myr. Similarities in the ages and compositions between the Mt. Edgar granite complex and the Panorama Formations[76] suggest that they were co-magmatic; the Panorama Formation (felsic volcanics) represents the eruptive phase of the granitic magmas that formed the Mt. Edgar granite complex. We estimate that the felsic volcanic rocks (i.e., the Panorama Formation) were accumulating at least 5 km in thickness on top of the Mt. Edgar granite complex (i.e., the lithostatic pressures of >1.5 kb) in order for granite magmas to crystallize without acquiring porphyritic textures[77]. Thus, toward the end of the accumulation of the thick Panorama Formation, the entire eastern part of the East Pilbara Terrane, from the Mt. Edgar area to the North Pole Dome area (~100 km W of Marble Bar) would have become subaerial at ~3,430 Ma. Regional erosion continued for ~80 Myr until the region became under a shallow sea and deposited the Strelley Pool Chert at ~3,350 Ma [66].

The questions of whether the continental crust existed beneath the Warrawoona Group igneous rocks and the origin of the granitic magmas for the Mt. Edgar Batholith have been debated. Some researchers[21,78-80] have suggested the thick submarine volcanic rocks of the Warrawoona Group accumulated on an older sialic continental crust, implying that the large granitoid magmas that formed the Mt. Edgar batholith and the volcanic Panorama Formation

682 were produced by the melting/assimilation of the older continental crust by mantle-derived
683 basaltic magmas. However, the available isotopic- and chemical data on zircons and igneous
684 rocks in the Pilbara district [78-80] are inconclusive for the origin of the granitoid-magmas in the
685 Pilbara district. If the granitoid magmas had been generated via either by the fractional
686 crystallization of basaltic magmas or by the melting/assimilation of continental crust, we would
687 expect the volumes of granitic magmas to have been much smaller than those of basaltic
688 magmas. However, the volume of the Mt. Edgar granitoids and the Panorama volcanics are too
689 large to have been produced by the Apex Basalt magmas, either by fractional crystallization or
690 by assimilation of the continental crust. A more likely scenario for the origin of the large felsic
691 magmas in the Apex Impact Crater would have been by 1-50 % partial melting of the deep
692 mantle peridotites by the asteroid impact (see Fig. 2c).

693 **B. Origin of the Ti-rich fragments in the Apex Basalt**

694 Titanite and rutile are common low-temperature alteration minerals in submarine basalts [27,
695 28], where Ti-rich iron-oxides, such as ilmenite ($FeTiO_3$) and titaniferrous magnetite, reacted
696 with Ca^{2+}-rich hydrothermal fluids, such as:

697 $$3FeTiO_{3(s)} + 3SiO_{2(aq)} + 3Ca^{2+} + 3H_2O + 1/2O_{2(aq)} = 3CaTiSiO_5 + Fe_3O_{4(s)} + 6H^+ \quad \text{(R-2)}$$

698 Such reactions produce magnetite and/or haematite as well as titanite. Submarine hydrothermal
699 fluids are products of seawater-rock interactions as seawater circulate through the underlying
700 rocks that are heated by an intrusive igneous body [62]. Temperatures of hydrothermal fluids that
701 discharge onto the seafloor near a heat source generally increase with time from ~50 °C to the
702 maximum of ~200-450 °C, depending on the initial temperature and size of the intrusive, and
703 then decrease (i.e., waning) to <50 °C. Low-temperature (T< ~100°C) submarine hydrothermal

fluids are typically enriched in Ca compared to the seawater [62], which promotes formation of titanite via R-2.

In contrast, high-temperature submarine hydrothermal fluids are typically poor in Ca [62]. Therefore, titanite does not form through R-2. Instead titanite would lose its Ca and form rutile via:

$$CaTiSiO_{5(titanite)} + 2H^{+} = TiO_{2(rutile)} + Ca^{2+} + SiO_{2(aq,s)} + H_2O \qquad \text{(R-3)}$$

The behaviors of Ca and Fe in titanite crystals and their host rocks in the ABDP #1 core (ED Figs. 5 a-m), especially in the chert/basalt mixed zone (~190–215 m depth zone), clearly indicate that the Ti-rich grains in the Apex Basalt and tsunami deposits were not produced by reaction R-2, but they were incorporated in the tsunami deposits and basalts as foreign grains, most likely as meteoritic minerals, and subsequently lost Ca via reaction R-3.

C. Approaches

To examine the validity of the above suggestions (A) and (B), we have carried out the following investigations: (i) field investigations of the impact structures and tsunami deposits; (ii) microscopic investigations of impact textures (e.g., shock-metamorphic features) in the MBCM and Duffer Formation; (iii) mineralogical and geochemical investigations of "meteoritic minerals" in the tsunami deposits, as well as in the Apex Basalt; (iv) geochemical investigations of the tsunami deposits and hydrothermally-altered Apex Basalt; and (v) thermochemical analyses of the stability and abundances of solid- and gaseous phases from solar-gas clusters.

C-1. *Field investigations*: Since Yr. 1999, we have carried out eleven field excursions/surveys to study the geology of the East Pilbara Craton, focusing specifically on banded iron formations, volcanogenic massive sulfide deposits, paleosols and the Marble Bar Chert/Jasper. During the field work in the Marble Bar area in 2018, we utilized a drone (DJI Mavic Pro) equipped with a high-resolution (4k) camera to investigate the distributions and structures of highly fragmented MBCM and the impact-induced tsunami deposits.

C-2. *Petrography and optical microscopy*: Optical microscopy lends itself to characterize Ti-Ca-Si-O-rich meteorite fragments under a microscope, especially their khaki-colour and

731 angular shapes. Therefore, it is not difficult to recognize the Ti-rich fragments on the surfaces of
732 the drill core using a hand lens or a binocular microscope. We have examined the entire ~265 m-
733 long ABDP #1 core for the presence/absence of meteorite fragments and, confirmed the
734 ubiquitous presence of Ti-rich fragments throughout the Apex Basalt section, from ~190 to ~265
735 m depths in the core section. The occurrences of meteoritic minerals in the selected 54 core chips
736 were photographed through optical microscopes under normal light at The Pennsylvania State
737 University (PSU). Morphologies of meteoritic grains in approximately 30 specimens (core chips,
738 polished sections, thin sections) were further examined under high-resolution microscopes by
739 Drs. Janine Diez and Walter Engel of the GRL, Inc. in Bern, Switzerland.
740 **C-3.** ***Bulk-rock chemical analyses***: The abundances of the major-, trace-, REE-, and
741 precious-elements in 70 chips of the volcanic rocks (basalt, komatiite, dacite) and 142 chips of
742 the Marble Bar Chert were analyzed by the Activation Analysis Ltd., Ontario, Canada, and by
743 the Mineral Constitution Laboratory of the Pennsylvania State University (see the data in
744 Supplementary Table 1). The bulk-rock chemical analyses have identified the zones of tsunami
745 deposits and hydrothermal alteration (ED. Figs. 5 a-f; 7 a-f).
746 **C-4.** ***Chemical analyses by X-ray fluorescence spectroscopy***: Spot analyses for the
747 concentrations of O, Mg, Al, Si, K, Cr, S, Ca, Ti, V, Mn, Fe, Ni, Cu, Zn, Co, Ga, Ge, Ir and Pt
748 were carried out on 21 spots on of un-polished core surfaces of Sample 257.1m, 29
749 spots on 213.10m, and 54 spots on 236.5m using an X-ray fluorescence spectroscopy
750 (XGT-5000 by Horiba, Inc.) at the PSU Geosciences Dept with a beam size of 10 μm. In
751 addition, elemental distribution maps of 6 areas (ranging from 1x1 to 5x5 mm in sizes) were
752 carried out using a 100 μm-size beam (see the data in Supplementary Table 2).
753 **C-5.** ***Chemical analyses by electron microprobe analyzers (EPMA)***: WDS analyses were
754 performed with a CAMECA SX-Five electron microprobe at the PSU Materials Characterization
755 Laboratory. The beam was regulated at 15kV 30nA with a spot size of 1 μm. A total of 580
756 spots on 10 samples were collected: 12 spots on Sample 259.95, 189 spots on 257.1, 41 spots on
757 236.6, and 40 spots on 214.43. Additionally, 55 spots on 259.95, 10 spots on 569, 220 spots on
758 214.43, 2 spots on 213.74, 3 spots on 213.3, 4 spots on 211.22, and 4 spots on 211 were analyzed
759 using a field emission scanning electron microscopy (FESEM, JSM-7001F) at Tohoku
760 University. In addition, approximately 30 elemental maps (ranging from 10x10 μm to 5x5 mm in

761 areal sizes) were constructed on the above samples. Samples for the EPMA analyses at PSU
762 were first coated with iridium to determine the contents of C, as well as O, Na, Mg, Al, Si, P,
763 S, K, Ca, Ti, V, Cr, Mn, Fe, Ni, Cu, and Zn. Subsequently, samples 259.95 and 214.43
764 were re-polished, re-coated with carbon, and analyzed for Ag, Au, Pt, Ir and Pb,
765 as well as the above major and trace elements. Samples for the FESEM analyses at
766 Tohoku were coated with carbon (see the data in Supplementary Table 3).
767 **C-6.** ***High resolution electron microscopy***: Sample powders for HRTEM (high-resolution
768 TEM) analyses were isolated and collected from microscopy thin sections, sample blocks and
769 from selected rock chips using a needle to lift material grains, crystal assemblages and lamellae
770 under a 8x-50x track stand stereo zoom parfocal trinocular microscope. The sample
771 powders were dispersed on 200 mesh Formvar/carbon coated copper or nickel grids and
772 examined in analytical microscopy at the University of Kentucky and NIOSH (JEOL 2100F
773 field emission transmission and scanning transmission microscope (TEM/STEM using an
774 analytical probe with 0.17 nm resolution) at 200 kV with Gatan Ultrascan 4k x 4k CCD camera,
775 Gatan Digital Micrograph software, Digiscan II, Gatan HAADF (high Angle Annular Dark
776 Filed) detector and Gatan 2000 Image Filter and at Wright Patterson Research Lab using a FEI
777 Titan Aberration-corrected (S)TEM. Energy dispersive spectroscopy (EDS) and electron energy
778 loss spectroscopy (EELS) analysis (Oxford Aztec EDS system, was used for elemental mapping
779 and EELS spot analysis and trace lines were obtained with a 1 nm probe, alpha of 12 mrad and
780 beta of 6 mrad; elemental intensity maps were obtained from core edge intensity acquired after
781 background subtraction using an integration window ranging from 10-30 eV. The oxidation state
782 for Ti in select grains was determined by EELS and compared to the Ti^{3+}/ Ti^{4+} ratio of synthetic
783 standard samples (the valence state of Ti was measured by means of EELS using a 200 keV
784 beam intensity and a Gatan PEELS 666 parallel-recording electron spectrometer (calibration
785 technique used intensity lines and spectral features of the L3,2 white lines of Ti (with a
786 resolution of 0.75 eV) which provides a direct determination of the Ti^{3+}/ Ti^{4+} ratio in nano-sized
787 grains. A Thermo Scientific FEI Talos F200S/TEM was used at WPAF Lab for fast EDS
788 mapping of nanoscale grains to minimize beam/sample interactions in 85 powdered samples
789 from Ti-rich sections of 210, 211, 213, 214.43, 218 and, 236.6. Elemental maps generally took
790 one to two minutes to acquire with a sensitivity great enough to detect elemental concentrations
791 in 3 nm size particles. A cryo-stage was also used to prevent heating of temperature-sensitive

792 sample grains and was operated with a Gatan CT3500 single tilt system with a tilt capability of
793 65 degrees.
794 **C-7. *Thermochemical analyses***: The thermodynamic calculations of crystallization history
795 of minerals and gaseous species during cooling of a hypothetical solar-gas cluster were carried
796 out with the following assumptions: (i) the system (gases + solids) remained closed; (ii) the
797 mineral- and gaseous species are in chemical equilibrium at all time; (iii) the bulk composition of
798 the system had the elemental abundance ratios of the Apex Asteroid (Table 1) and the H/C/Si
799 ratios of the Solar System estimated by Lodders[1]; and (iv) the total gas pressure was 10^{-4} atm.
800 Previous researchers[1,52] have adopted the elemental ratios of the carbonaceous chondrites, which
801 are similar to the current Solar Wind, and the total gas pressure of 10^{-4} atm in their
802 thermodynamic computations of the crystallization history of the Solar System. We have
803 computed the condensation/transformation/disappearance temperatures of nearly 700 compounds
804 as a function of temperature using the software package Thermo-Calc [81] with the SSUB4
805 database [82] developed by means of the CALPHAD method [83,84]. In the CALPHAD method,
806 the Gibbs energy function of each individual phase is modeled as a function of temperature,
807 pressure, and composition. The equilibrium state of a system and its change with respect to
808 temperature, pressure, and composition are obtained by the minimization of the Gibbs energy of
809 the system, and the equilibrium state is represented by the co-existing phases and their respective
810 compositions and quantities. In the present computations, all phases are treated as stoichiometric
811 compounds except the gas phase which consists of over 300 species and is treated as ideal gas.
812 Thermodynamic calculations for the selected redox reactions (Fig. 6c) were carried out using the
813 method in Ohmoto[66] and thermodynamic data in Supplementary Table 5.
814
815 **References for Methods only**

816 59. Addison, W.D. et al. Discovery of distal ejecta from the 1850 Ma Sudbury impact event.
817 *Geology* **33,** 193-196 (2005).
818 60. Cannon, W.F., Schulz, K.J., Horton, J.W. Jr. & Kring, D.A. The Sudbury impact layer in the
819 Paleoproterozoic iron ranges of northern Michigan. *GSA Bull.* **122,** 50-75 (2010).

61. Elders, W.A. et al. Origin of a rhyolite that intruded a geothermal well while drilling at the Krala volcano, Iceland. *Geology* **39,** 231-234 (2011).

62. Ohmoto, H. Formation of volcanogenic massive sulfide deposits: The Kuroko perspective. *Ore Geol. Rev.* **10**, 135-177 (1996).

63. Samieyani, A. Mineralogy and geochemistry of ~3.5 Ga volcanogenic massive sulfide deposits at the Big Stubby prospect, the Pilbara district, Western Australia. *Thesis* Tohoku University (1995).

64. Li, W., Johnson, C.M. & Beard, B.L. U-Th-Pb isotope data indicate phanerozoic age for oxidation of the 3.4 Ga Apex Basalt. *EPSL* **319-320,** 197-206 (2012).

65. Rasmussen, B., Krapez, B. & Muhling, J.R. Hematite replacement of iron-bearing precursor sediments in the 3.46-b.y.-old Marble Bar Chert, Pilbara craton, Australia. *GSA Bull.* **126,** 1245-1258.

66. Ohmoto, H. A seawater-sulfate origin for early Earth's volcanic sulfur. *Nature Geosci.* **13,** 576-583 (2020).

67. Hughes, D.W. The approximate ratios between the diameters of terrestrial impact craters and the causative incent asteroids. *Mon. Not. R. Astro. Soc.* **338,** 999-1003 (2003).

68. Ingle, S. & Coffin, M.F. Impact origin for the greater Ontong Java Plateau? *EPSL* **218,** 123-134 (2004).

69. Takahashi, E. & Scarfe, C.M. Melting of peridotite to 14 GPa and the genesis of komatiite. *Nature* **315,** 566-568 (1985).

70. Hirose, K. & Kushiro, I. Partial melting of dry peridotite at high pressures: Determination of compositions of melts segregated from peridotite using aggregates of diamond. *EPSL* **114,** 477-489 (1993).

71. Rutherford, M.J. & Gardner, J.E. Rates of magma ascent. *Encyclopedia of Volcano* 207-218 (Academic Press 2000).

72. Smetannikov, A.S. High temperature hydrodynamics of explosion and shock wave phenomena. *Nonlinear Phenomena in Complex Systems* **17,** 439-444 (2014).

73. Bryan, S.E. & Ernst, R. Revised definition of large igneous provinces (LIPs). *Earth-Sci. Rev.* **86,** 175-202 (2007).

74. Kring, D.A. et al. Chcxulub and the exploration of large peak-ring impact craters through scientific drilling. *GSA Today* **27,** doi: 10.1130/GSATG352A.1. (2017).

75. Grieve, R.A.F. The Sudbury Structure: Controversial or misunderstood? J. Geophys. Res. **96,** 22,753-22,764 (1991).

76. Smithies, R.H., Champion, D.C., Van Kranendonk, M.J. & Hickman, A.H. Geochemistry of volcanic rocks of the northern Pilbara Craton, Western Australia. Western Australia Geological Survey Rept. **104,** 1-47 (2007).

77. Burnham, C.W. & Ohmoto, H. Late-stage processes of felsic magmatism. *Granitic Magmatism and Related Mineralization Mining Geology Sp. Issue* 1-11 (1980).

78. Collins, W.J. Melting of Archaean sialic crust under high a_{H2O} conditions: genesis of 3300 Ma Na-rich granitoids in the Mount Edgar Batholith, Pilbara Block, Western Australia. *Precambrian Res.* **60,** 151-174 (1993).

79. Van, Kranendonk, M.J. et al. Evidence for Mesoarchean (~3.2 Ga) rifting of the Pilbara Craton: The missing link in an early Precambrian Wilson cycle. *Precambrian Res.* **177,** 145-161 (2010).

80. Kemp, A.I.S., Hickman, A.H., Kirkland, C.L. & Vervoort, J.D. Hf isotopes in detrital and inherited zircons of the Pilbara Craton provide no evidence for Hadean continents. *Precambrian Res.* **261,** 112-126 (2015).

81. Andersson, J. O. et al. THERMO-CALC & DICTRA, computational tools for materials science. CALPHAD **26**, 273–312 (2002).

82. Scientific Group Thermodata Europe (SGTE). SSUB5: SGTE substance database. Available at: http://www.thermocalc.com/media/10097/ssub5.pdf.

83. Kaufman, L. & Bernstein, H. *Computer Calculation of Phase Diagram*. (Academic Press Inc., 1970).

84. Liu, Z. K. First-Principles calculations and CALPHAD modeling of thermodynamics. *J. Phase Equilibria & Diffus*. **30**, 517–534 (2009).

Acknowledgements We would like to thank W.W. Engel and J.G. Diez for assistance in microscopic investigations; K.L. Crispin and H. Saito for assistance in EPMA analyses; S. Karduck, Y. Kunitake, R. Yamada, M. Gonzales and L.J. Liermann for assistance in laboratories; K. Tsukamoto, P.J. Steinhardt and A. Dozier for discussion on meteorites; and D. Eggler, L.S. Hollister, A. Rose, H. Naraoka, K. Spangler, A. Dilla, D. Gold, G. Gross, J. Lockwood and W. Alvarez for comments on an earlier manuscript. Special thanks are due to A. Hickman for geological information and support throughout the course of this study. Research funding for this study was provided by the NASA Astrobiology Institute (CA#NNNA04CC06A & CA#NNA05GK00G) and The Pennsylvania State University to H.O.; by National Science Foundation through Center for Computational Materials Design (IIP-1034965) to Z.K.L.

Author contributions U.M.G. discovered the first Apex Asteroid fragment (Fig. 4a) in the ABDP #1 drill core and carried out mineralogical and chemical investigations of the various minerals utilizing a variety of electron microscopes. A.C., Y.T., Y.W., H.H. and H.O. carried out the 2018 field survey; Y.T. and H.O. conduced the mineralogical and chemical investigations utilizing optical microscopes and EPMA; and Z.K.L. and H.O. performed the thermodynamic

modelings. H.O. coordinated this research and wrote the entire paper. All the authors discussed the results and commented on the manuscript.

Competing interests

The authors declared no competing interests.

Data availability

Methods, Extended Data and Supplementary Information are available in the online version of the paper. Source data are provided with this paper.

Additional information

Correspondence and requests for materials should be addressed to H.O.

Extended Data for

"Discovery of a 3.46 billion-year-old impact crater in Pilbara, Western Australia"

By: H. Ohmoto, U.M. Graham, Z-K. Liu, Y. Tsukamoto, Y. Watanabe, H. Hamasaki & A. Chorney

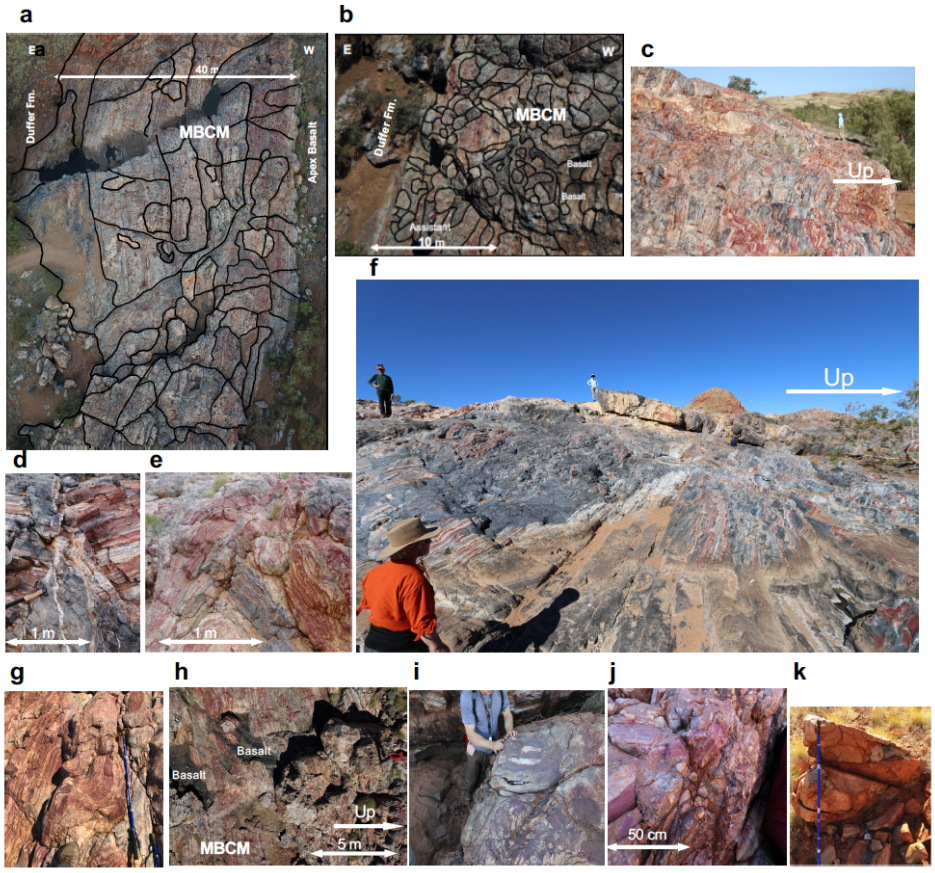

ED Figure 1. Asteroid impact structures in the Marble Bar Chert Member (MBCM). (a) & (b): Aerial (drone) photos of the shattered MBCM from ~250 m above the ground at immediately south of the Marble Bar Pool. Note that the fractures (as wide as ~5 m) run mostly oblique to the MBCM's bedding planes, and that the brecciated fragments (as large as ~10 m) were rotated and dislocated. The black fine-grained sediments (i.e., tsunami sediments) filled the fractures and gaps between the fragments. (c)-(j): Impact-induced tsunami deposits in the Marble Bar Pool area. Notice the various-sized fragments of the MBCM, soft-sediment deformation, incorporation of the Apex Basalt in the chert-rich sediments (b & h) and incorporation of chert fragments in basalts (i & j). (k): Variable sized, mostly rounded blocks and fragments of volcanic rocks of the Duffer Fm. in matrices comprised of fine-grained volcanic rocks at ~4 km SE of the Lennon's Find (Fig. 1c). The tsunami deposits (~15 m thick) in this area lack fragments of the MBCM, because it did not form in this area.

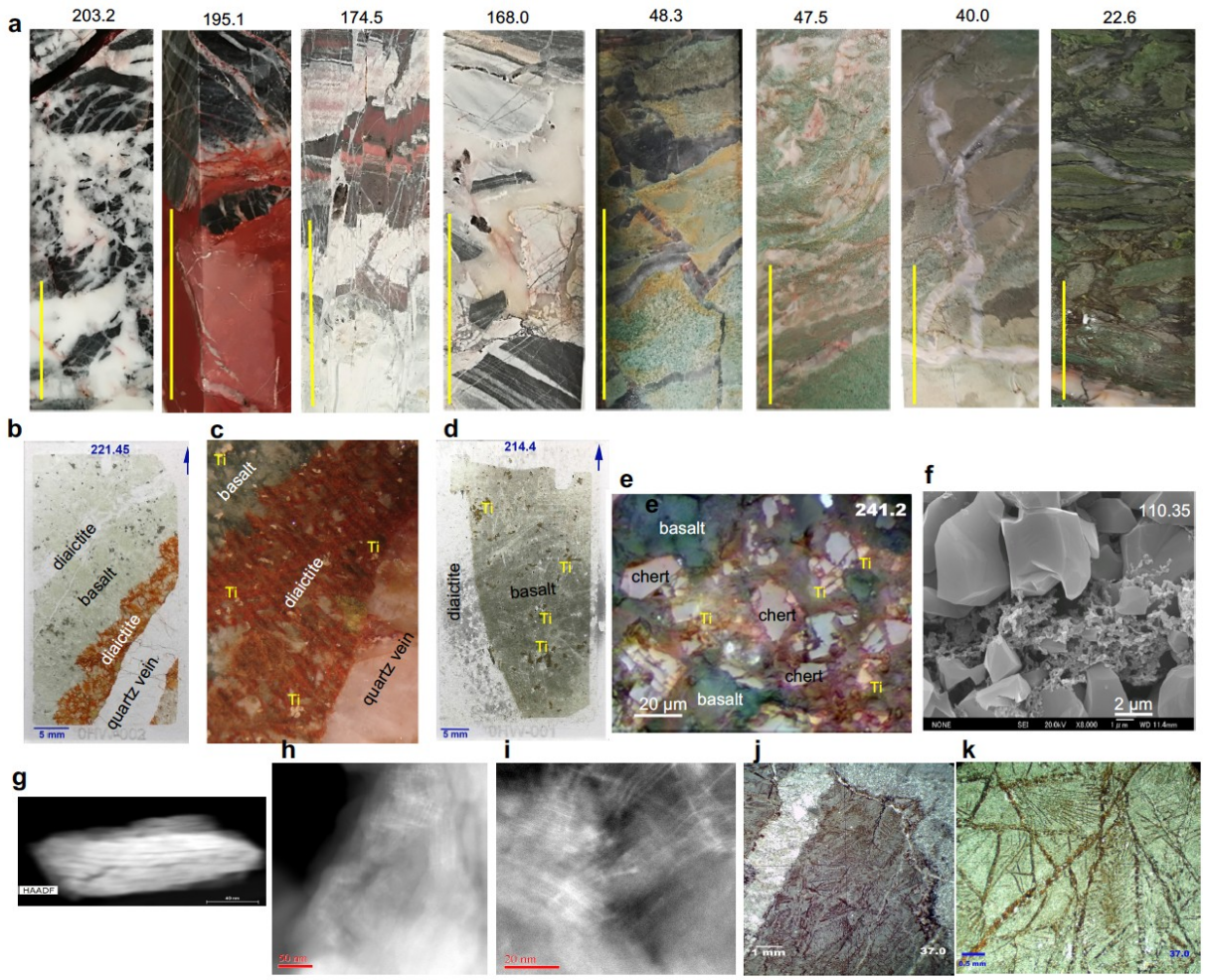

ED Figure 2. Impact-induced textures in the MBCM and the Duffer Formation. (a): Photos of selected drill core sections from the ABDP #1 hole, showing the impacted rock textures (fractures, dislocations, veins, fragments) in the MBCM (203.2 – 165.4 m depths) and the Duffer Formation (48.3 – 22.6 m). The yellow scale-bars represent 5 cm. (b)-(e): Thin section photos of the mixtures of basalt- and chert-fragments in the tsunami zone of the ABDP drill core. "Ti" represents Ti-rich fragments. (f): A thin section photo of "crushed chert fragments and powders" of the Marble Bar Chert. (g)-(i): HAADF photos of nano-scale stress-features in a chert sample from 171 m depth. (j)-(k): Thin section photos (under reflected light) of Spinifex textures and a quartz-bearing micro vein in the Duffer Formation.

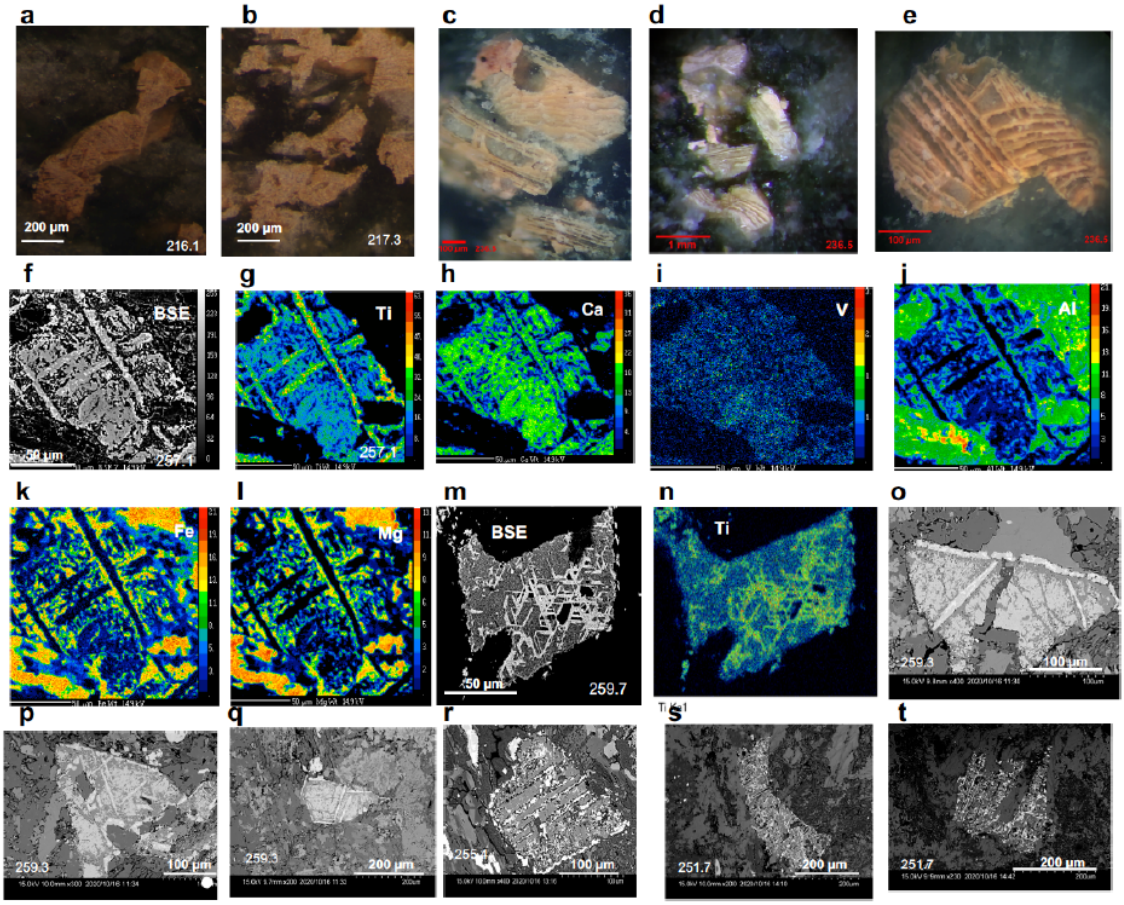

ED Figure 3. Morphologies, textures and compositions of Ti-rich asteroid fragments. (a)-(e): Microscope photos (under reflected light) of Ti-rich fragments on unpolished drill-core surfaces. (f)-(l): BSE and elemental maps of a Ti-rich fragments (Ti-, Ca- and V-rich) in basalt (Al-, Fe and Mg-rich) from 257.1 m depth. (m) & (n): BSE and Ti-map of a Ti-rich fragment in basalt at 259.7 m. (o)-(t): BSE photos of Ti-rich fragments in Apex Basalt of the ABDP #1 core.

914

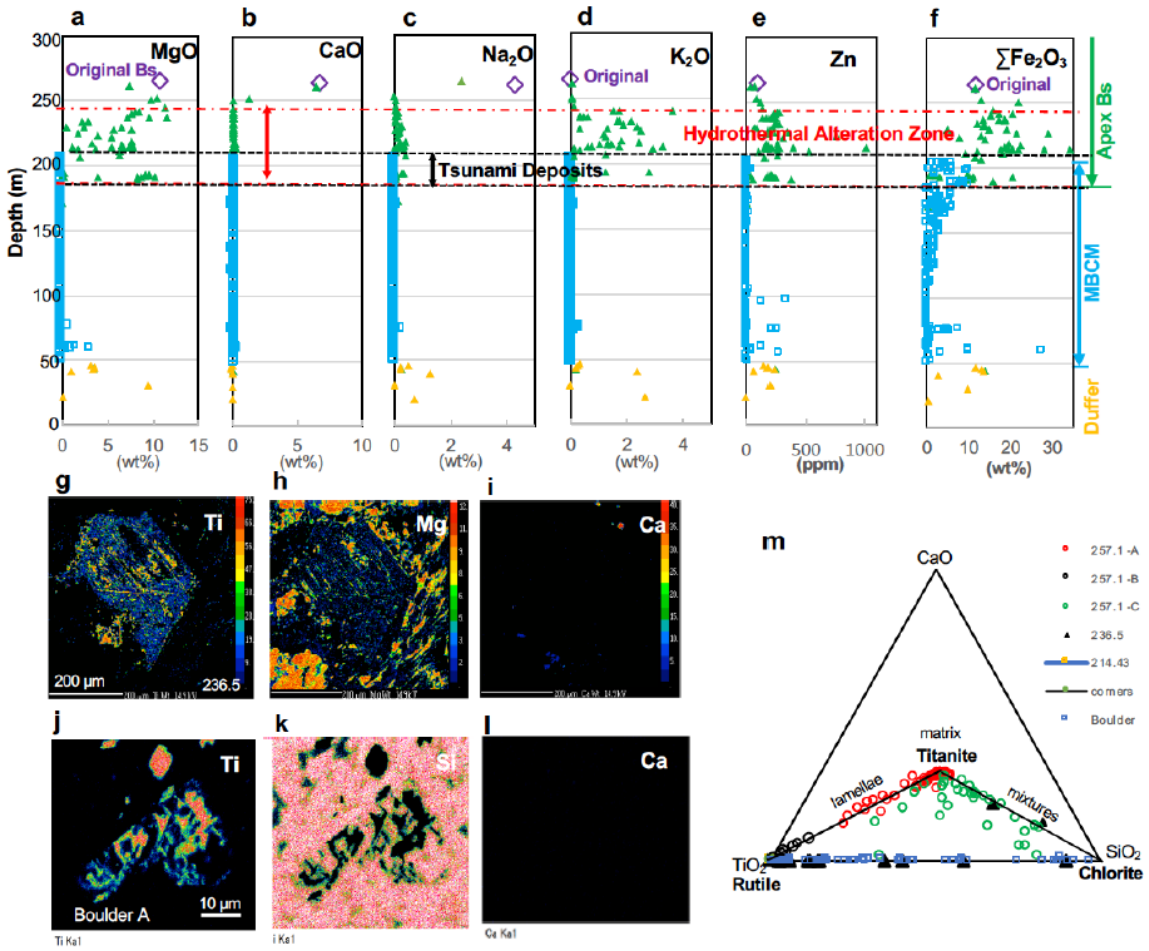

ED Figure 4. Submarine hydrothermal alteration of the basalt and the tsunami deposits in the ABDP #1 core. (a)-(f): Bulk-rock chemical compositions of the drill-core samples, indicating that the tsunami deposits and the lower part of the Apex Basalt exhibit the characteristics of rocks that were altered by high-temperature (>150°C) submarine hydrothermal fluids, including the losses of Ca and Na and additions of K, Zn & Fe. (g)-(i): EPMA maps of Ti-rich fragments in hydrothermally-altered basalt and tsunami deposits, showing the losses of Ca. (m): EPMA spot analyses of Ti-rich grains, indicating that the matrices of unaltered grains are comprised of titanite or titanite-silica mixtures, the lamellae of mixtures of titanite and rutile, and the altered grains are essentially Ca-free.

915

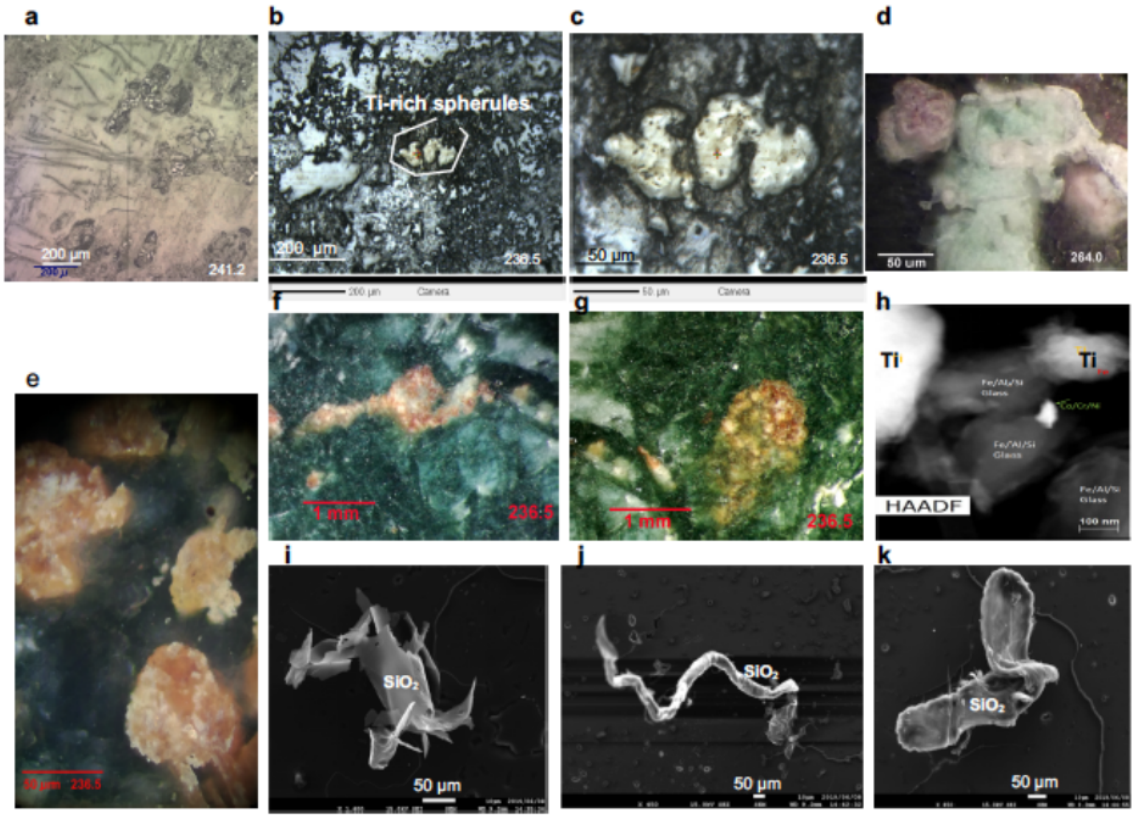

ED. Figure 5. Meteoritic and terrestrial materials that possibly formed in the impact clouds. (a)-(d): Titanite-rich spherules with rutile lamellae, which probably formed by the melting of Ti-rich angular fragments in the impact clouds. (e)-(g): Microscope photos of spherules of basalt melts with inclusions of Ti-rich meteoritic grains. (h): A HAADF photo of basaltic melt spherules with Ti-rich fragments. (i)-(k): Products of condensation of SiO_2-rich vapor, which was probably generated by the asteroid impact to the MBCM, in the impact clouds.

916

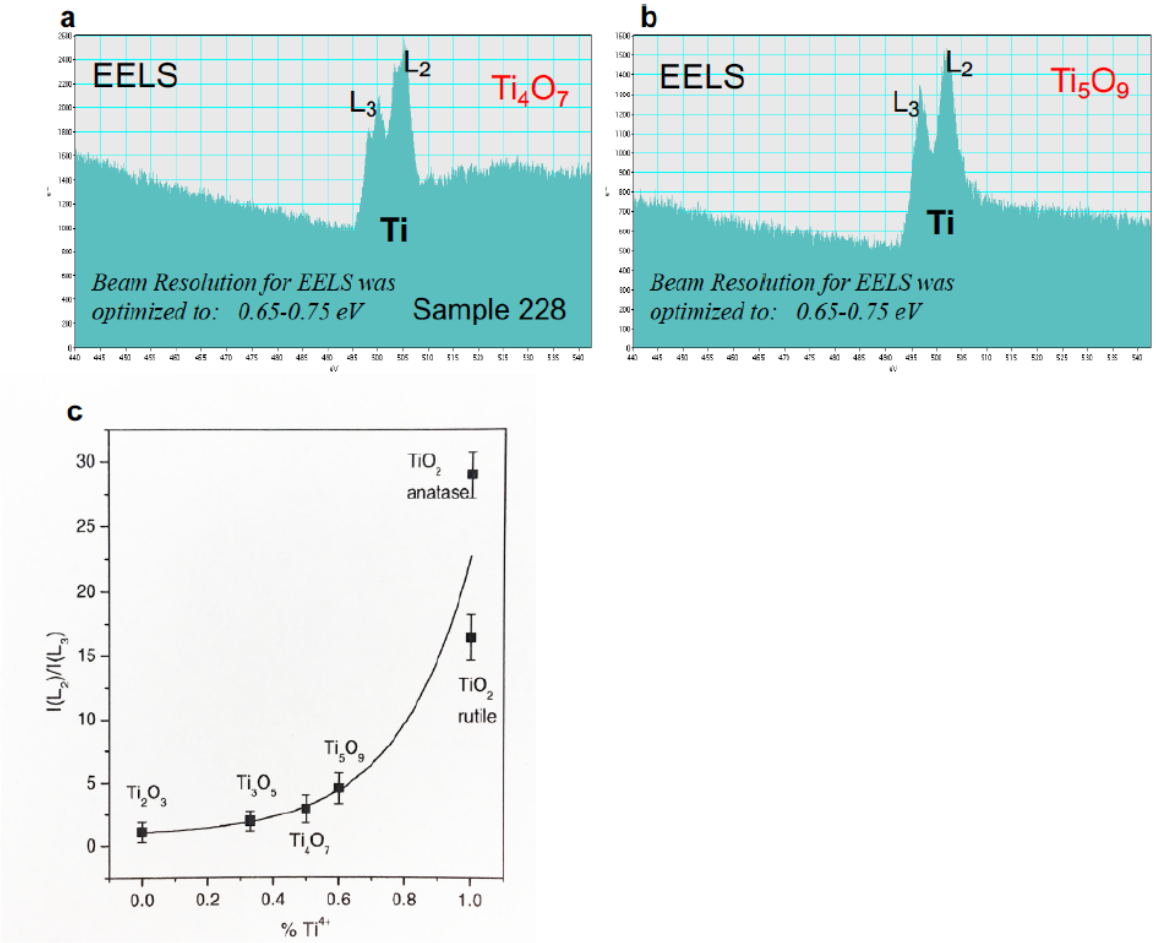

ED Figure 6. Oxidation state of Ti in the Ti-rich fragments. (a) & (b): EELS analyses of Ti atoms in "rutile" grains have revealed the presence of Ti^{3+} as well as Ti^{4+} in the forms of Ti_4O_7 and Ti_5O_9 molecules. (c): Relationships between the $Ti^{4+}/\sum Ti$ ratios and L_2/L_3 ratios (after Stoyanov et al.[33]).

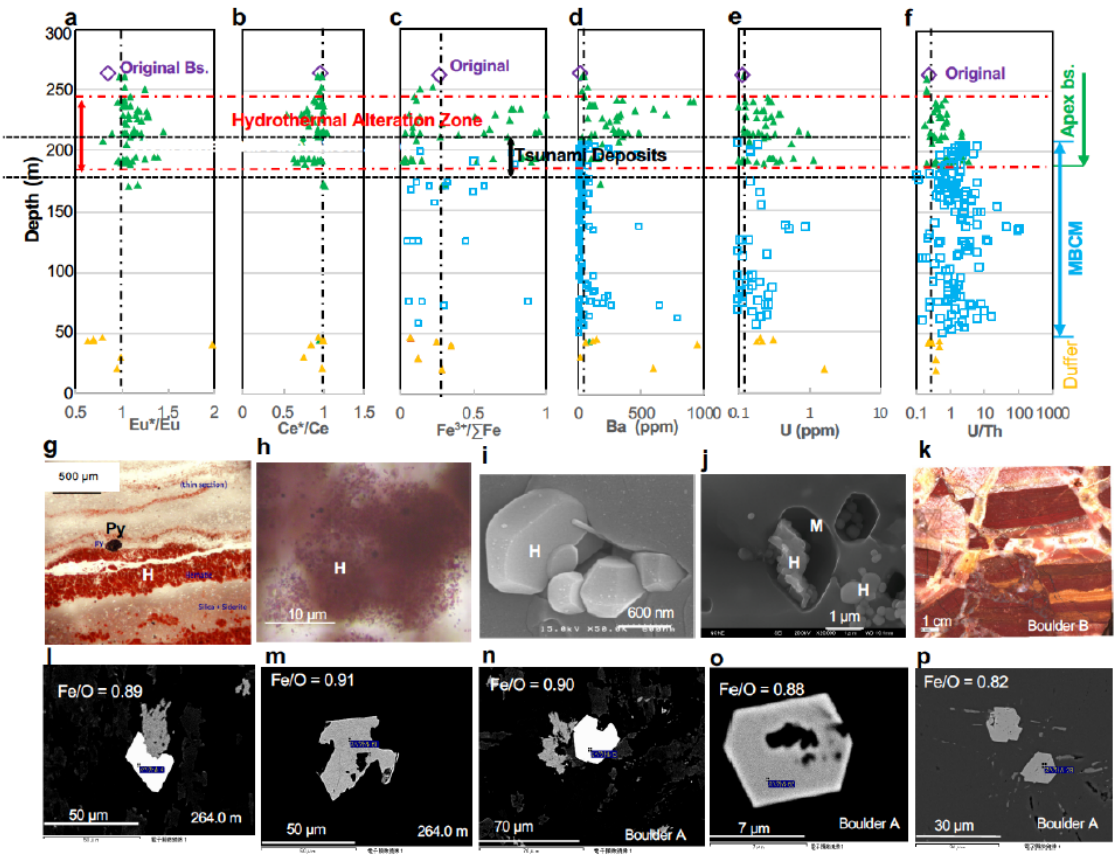

ED Figure 7. Involvements of O_2-rich deep-ocean water in: the formation of primary haematite in the MBCM; the alteration of the basalt and tsunami deposits; and the alteration of meteoritic minerals. (a)-(f): Evidence for the involvement of O_2- and SO_4^{2-}-rich ocean water in the alteration of the Apex Basalt and tsunami zone: negative Ce anomalies, increased Ba and U contents and increased $Fe^{3+}/\sum Fe$ and U/Th ratios of rocks in the hydrothermal alteration zone. (g)-(o): Microscopic and SEM images of sub-micron-sized primary haematite crystals in the MBCM (from Hoashi et al.[19]). (k): Fragmented red cherts in the tsunami deposits, clearly indicating that the haematite crystals in the MBCM formed prior to the asteroid impact. (l)-(p): SEM photos of meteoritic Fe-oxide crystals in the tsunami deposits, showing that they are more than 10 times larger than the primary ßhydrothermal haematite crystals (h-j) in size. Their original Fe/O ratios (~0.90) are similar to those of wüstite (FeO); the lower Fe/O ratios (e.g., 0.82) in some crystals (Supplementary Table 3) were probably due to the reactions with O_2-rich atmosphere and ocean at 3.46 Ga ago.

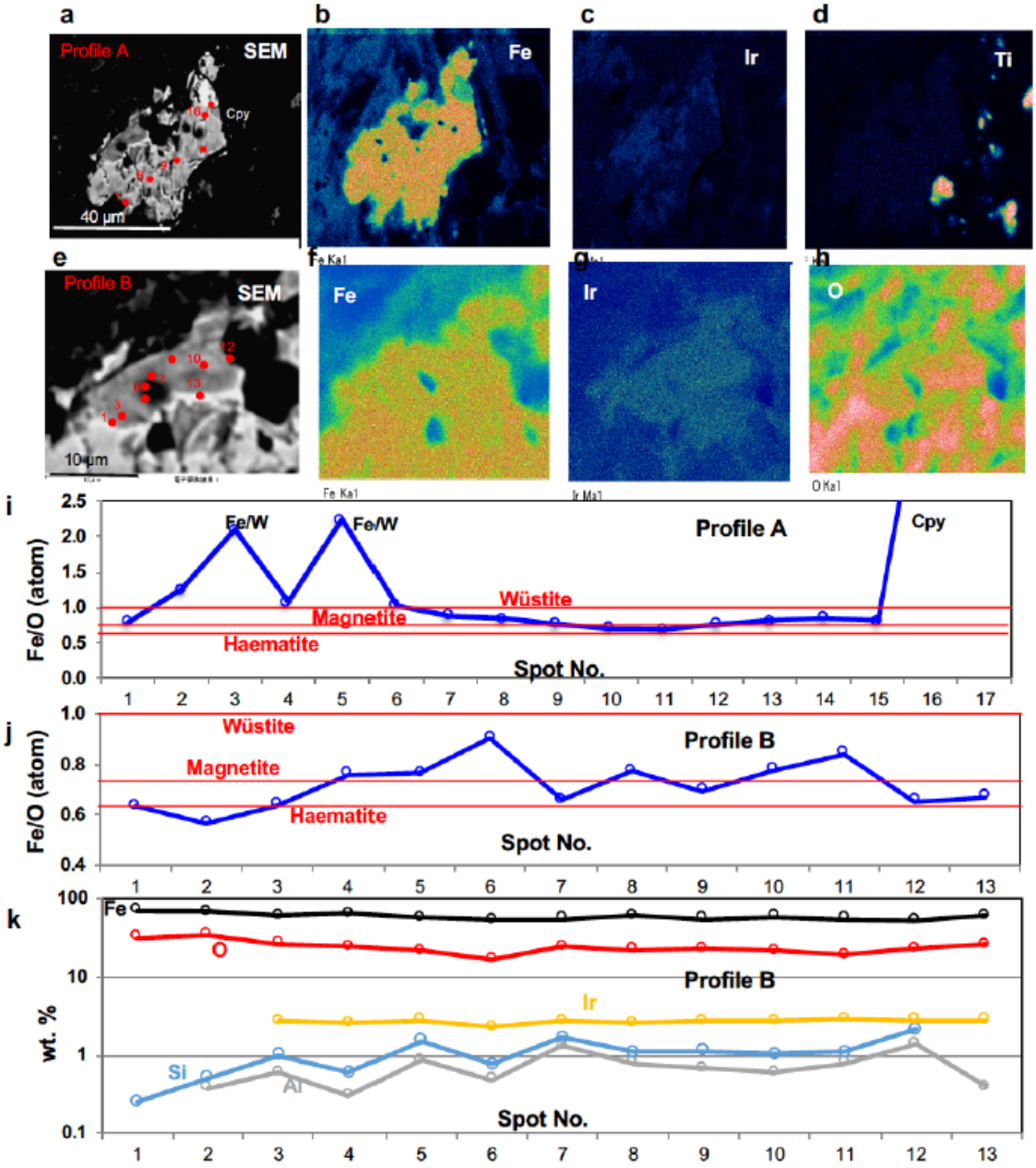

ED Figure 8. Iridium-rich Fe metal. (a)-(h): EPMA analyses of a ~50 µm-sized Fe-rich grain. (i): Variations in the Fe/O ratios along Profile A. (j): Variations in the Fe/O ratios along Profile B. (k): Concentration profiles of Fe, O, Ir, Si, and Al along Profile B. Variations in the Fe/O ratios in (i) and (j) suggest that the original phase in this part of the grain was metallic iron (Fe/O >>1) and possibly wüstite (FeO), and that the decreases in the Fe/O ratios less than 1 were due to the oxidation of Fe-metal and wüstite to magnetite and haematite during/after the passage through an oxygenated atmosphere and ocean.

919

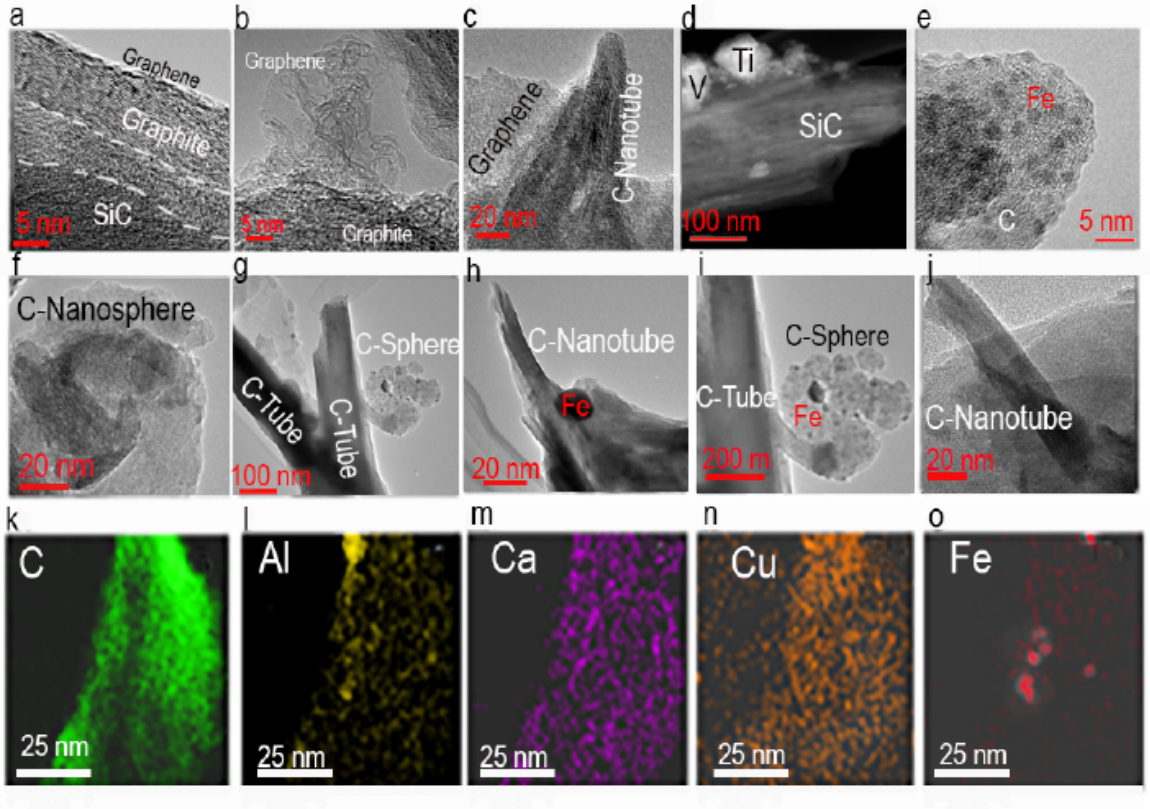

ED Figure 9. Carbon-rich phases from the Apex Asteroid. (a)-(j): Various carbon-bearing nanocrystals (graphene, tubular C, graphite and silicon carbide). (k)-(m): C/Al/Ca/Si/Cu alloys. Photos under HRTEM and HAADF (see C-6 in *Methods*).

920

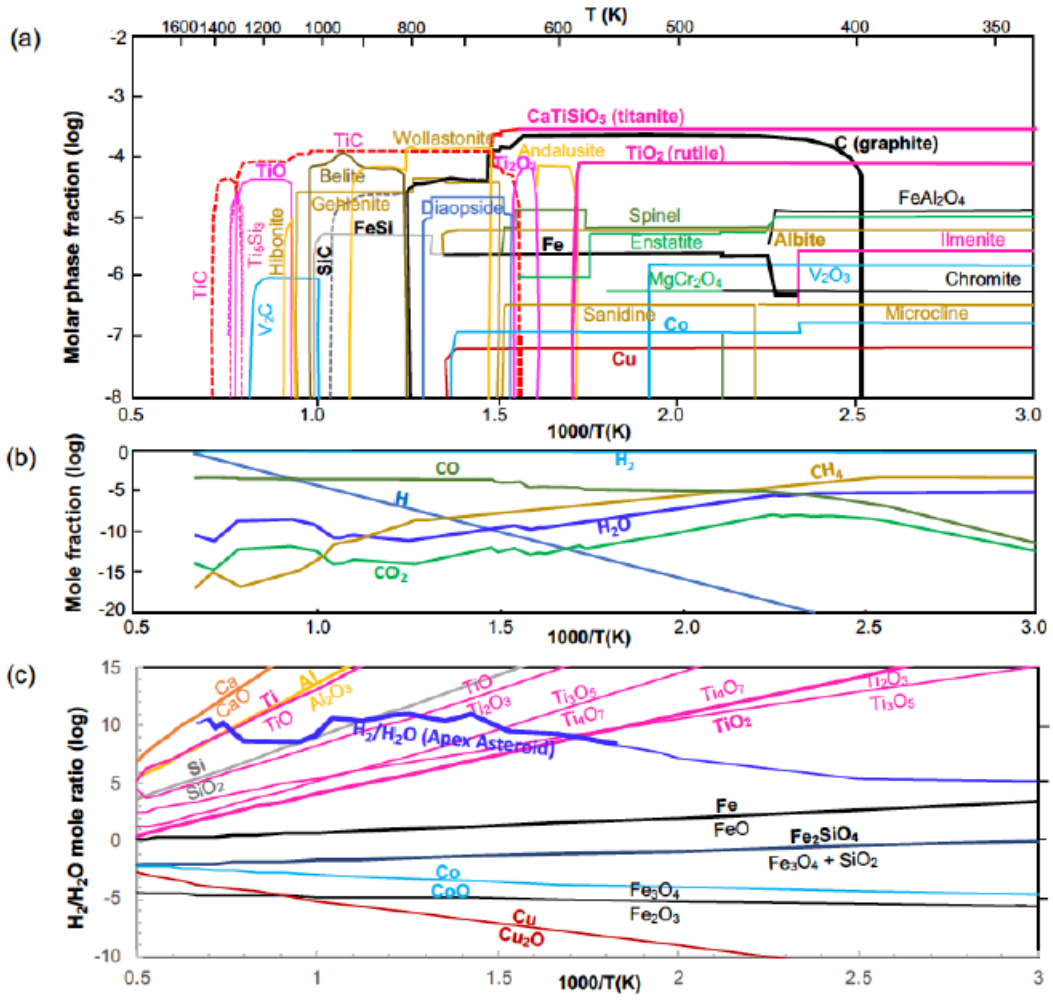

E.D.Figure 10. Thermochemical analyses of the formation conditions of the Apex Asteroid at $\sum P = 10^{-10}$ atm. (a): Temperatures for the condensation and transformation of minerals from a solar gas cluster ("the Apex gas cluster"). (b): Abundances of the major gaseous species in the Apex gas cluster. (c): Stability relationships among some redox-sensitive minerals as a function of H_2/H_2O ratio of the coexisting vapor phase and temperature. Superimposed is the change in H_2/H_2O ratio of the Apex gas cluster of (b).

921